UNIVERSIDADE
BEIRA INTERIOR

CFD Study of the Aero@UBI03 Shell Eco-Marathon 2019 Prototype

(Versão final após defesa)

Jorge Filipe Cardoso Rodrigues

Dissertação para obtenção do Grau de Mestre em

Engenharia Aeronáutica

(mestrado integrado)

Orientador: Prof. Doutor Miguel Ângelo Rodrigues Silvestre

Dezembro de 2021

Dedicatória

Quero dedicar esta dissertação e todo o meu percurso académico aos meus pais e aos meus avós e à minha família por me terem sempre apoiado e por me terem dado esta oportunidade!

Agradecimentos

Quero agradecer o Professor Doutor Miguel Ângelo Rodrigues Silvestre, orientador desta dissertação, por me ter dado esta oportunidade de trabalhar sobre o seu encargo.
Também queria agradecer a todos os meus amigos e às grandes amizades que forjei nestes últimos anos, e que me ajudaram no meu percurso académico e pessoal, especialmente à minha melhor amiga Kateryna Shvydyuk por me ter sempre apoiado, mesmo nos meus pontos mais baixos e por me fazer a pessoa quem sou hoje.

Resumo

Nos últimos 35 anos, a Shell tem organizado uma competição destinada a alunos com foco na otimização de veículos para a minimização do consumo de energia de veículos rodoviários, denominada Shell Eco-Marathon. O concurso viu ao longo dos anos melhoria progressiva nas escolhas de design, o que levou a novos recordes em eficiência energética. Na UBI, uma história semelhante aconteceu desde a primeira participação da equipa Aero@UBI na competição, em 2014. Em 2019, na sua terceira iteração de veículos, a equipa AERO@UBI03 conquistou o Prémio de Economia Circular e alcançou 612 km/kWh no evento principal, o sexto lugar na categoria de protótipo elétrico a bateria. Neste trabalho, foi realizada uma análise aerodinâmica completa ao protótipo Aero@UBI03 recorrendo à Dinâmica de Fluidos Computacional, com o *software OpenFOAM*, para avaliar o desempenho aerodinâmico do veículo na forma de áreas de arrasto e sustentação e os detalhes sobre o escoamento que possam motivar alterações futuras com vista à redução do consumo energético. Foi utilizado o modelo de turbulência *k*-ω*SST* e as funções de parede disponíveis no software *OpenFOAM*. Foi descoberto que o veículo produz uma esteira de quatro vórtices, dois gerados pelas carenagens das rodas dianteiras e os outros dois pelas mesmas carenagens mas no fundo do veículo. Também foi notado que o ponto de estagnação não parece estar numa posição ideal, pois cria uma queda de pressão excessiva na parte inferior do veículo. O protótipo resulta num SC_D de $0,03227$ m² e um SC_L de $-0,03835$ m². Mais estudos foram realizados ajustando a altura do veículo, bem como o ângulo de ataque. Estes mostraram que melhorias são possíveis, especialmente no desenho das carenagens, a fim de reduzir a sustentação negativa existente para um valor nulo.

Palavras-chave

Aerodinâmica, CFD, Shell Eco-Marathon

Abstract

Over the last 35 years, Shell has organized a student programme focused on road vehicles energy optimisation called Shell Eco-Marathon. The competition has seen over the years a lot of improvement in design choices which led to new records in energy efficiency. At UBI, a similar story has happened since its first participation in the competition in 2014. In 2019, in its third vehicle iteration, the AERO@UBI03 team won the Circular Economy Award and achieved 612 km/kWh at the main event, the 6th place in the battery electric prototype category. In this work, a full aerodynamic analysis using Computational Fluid Dynamics, with the software *OpenFOAM*, was performed to evaluate the flow, pressure contours, drag and lift using the *k*-ω*SST* turbulence model and wall functions available in the *OpenFOAM* software. It was discovered that the vehicle produces a four vortices wake, two generated by the front wheels fairings and the other two by the geometry of the vehicle. It was also noticed that the stagnation point was in a not optimal position as it creates a pressure drop when the flow moves to the underside of the vehicle. The prototype has a SC_D of 0.03227 m² and a SC_L of -0.03835 m². A few more studies were conducted by adjusting the height of the vehicle as well as the angle of attack. These showed that improvements were possible specially in the fairings design in order to reduce the existent downforce.

Keywords

Aerodynamics, CFD, Shell Eco-Marathon

Contents

List of Figures

List of Tables

List of Abbreviations

UBI	Universidade da Beira Interior
CAD	Computer Aided Design
CFD	Computer Fluid Dynamics
GUI	Graphical User Interface
RL	Refinement Level
SST	Shear Stress Transport
STL	Standard Tessellation Language
SEM	Shell Eco-Marathon

Nomenclature

δ_{ij}	Kronecker delta	
μ	Dynamic viscosity	$[\mathrm{kg\ (m \cdot s)^{-1}}]$
ν	Kinematic Viscosity	$[\mathrm{m^2\ s^{-1}}]$
ν_t	Turbulent visocity	$[\mathrm{m^2\ s^{-1}}]$
ω	Turbulent specific dissipation rate	$[\mathrm{m^2\ s^{-3}}]$
ω_{log}	ω computed by the inertial sublayer assumptions	
ω_{vis}	ω computed by the viscous sublayer assumptions	
ρ_∞	Freesteam Fluid density	$[\mathrm{kg\ m^{-3}}]$
τ_ω	Wall shear stress	$[\mathrm{Pa}]$
C_D	Drag Coefficient	
C_L	Lift Coefficient	
S_{ij}	Mean rate of strain tensor	$[\mathrm{N\ (m^2 \cdot s)^{-1}}]$
U_∞	Freestream Fluid Velocity	$[\mathrm{m\ s^{-1}}]$
C_μ	Turbulence model constant	
C_P	Pressure Coefficient	
I	Turbulent intensity	
k	Kinetic turbulent energy	$[\mathrm{m^2\ s^{-2}}]$
L	Vehicle length	$[\mathrm{m}]$
l	Turbulent length scale	$[\mathrm{m}]$
p	Pressure	$[\mathrm{Pa}]$
p_∞	Freestream Pressure	$[\mathrm{Pa}]$
Re	Reynolds Number	
S_w	Wetted Area	$[\mathrm{m^2}]$

SC_D	Drag Area	$[m^2]$
SC_L	Lift Area	$[m^2]$
u_*	Friction velocity	$[m\ s^{-1}]$
y	Distance from the wall	$[m]$
y^+	Nondimensional wall unit	
ρ	Fluid density	$[kg\ m^{-3}]$

Chapter 1

Introduction

Over the last 35 years, Shell has organized a student programme focused on road vehicles energy optimisation called Shell Eco-Marathon. The competition has seen over the years a lot of improvement in design choices which led to new records in energy efficiency. At UBI, a similar story has happened since its first participation in the competition in 2014. In 2019, in its third vehicle iteration, the AERO@UBI03 team won the Circular Economy Award and achieved 612 km/kWh at the main event, the 6th place in the battery electric prototype category.

When developing the prototype, because of the tight schedule of participation in the competition event, no previous aerodynamic studies could be made before the construction of the vehicle, hence the team had no clues to what the performance would be. Moreover, in order to improve the vehicle, the team would need quantitative and qualitative results such as aerodynamic drag, pressure contours and streamlines. With this work these will be gathered and analyzed such to improve the current and future prototypes.

The main goal of the present work was to evaluate the aerodynamic performance of the Aero@UBI03 Shell Eco-Marathon 2019 prototype. In order to study this, a methodology followed by a validation process using the Ahmed body was performed with the purpose of setting the correct parameters for the main simulation.

Soon after, the Aero@UBI03 simulation was ran. This involved setting up the CAD properly by closing any open surfaces and adding small 5 millimeter pads beneath the wheels to prevent cell skewness. Afterwards, a mesh was generated and all parameters were set as explained in chapter 3. Subsequent cases were also evaluated to have a better understanding of all the obtained results. All of these are present in chapter 4.

1.1 Shell Eco-Marathon Background

The Shell Eco-Marathon (SEM) is a competition created by the Royal Dutch Shell or ”Shell” oil and gas company as a global academic programme focusing on energy optimisation. With over 35 years of history, the programme has brought together thousands of Science, Technology, Engineering and Maths (STEM) students from all across the globe to create,

build and drive some of the world's most energy-efficient vehicles. The main core idea of the competition is how far one can go with one liter of fuel and from that idea many teams redefined the known limits introducing groundbreaking vehicles that shattered records such as the Pac Car II from ETH Zurich team in 2005 with a record consumption of 5385 km/l. The teams compete in two categories, prototype and urban concept where they branch out depending on the used energy type, such as internal combustion, electric or hybrid propulsion. In the former category, the focus is to create the most efficient vehicle possible (within rules) by minimizing the energy consumption, in the latter, practical road use designs are the goal.

1.1.1 UBI's SEM team background

At UBI the AERO@UBI team, comprising of aeronautical engineering students has participated since 2014 in the electric prototype vehicle category of the SEM Europe anual event. In the recent years, 2014 and 2015, the team entered the competition with the Aero@UBI01 vehicle, however an issue with the motor controller made it impossible to score a valid result in the first participation, in 2015, a 19th place was achieved with the 330.8 km/kWh consumption mark.

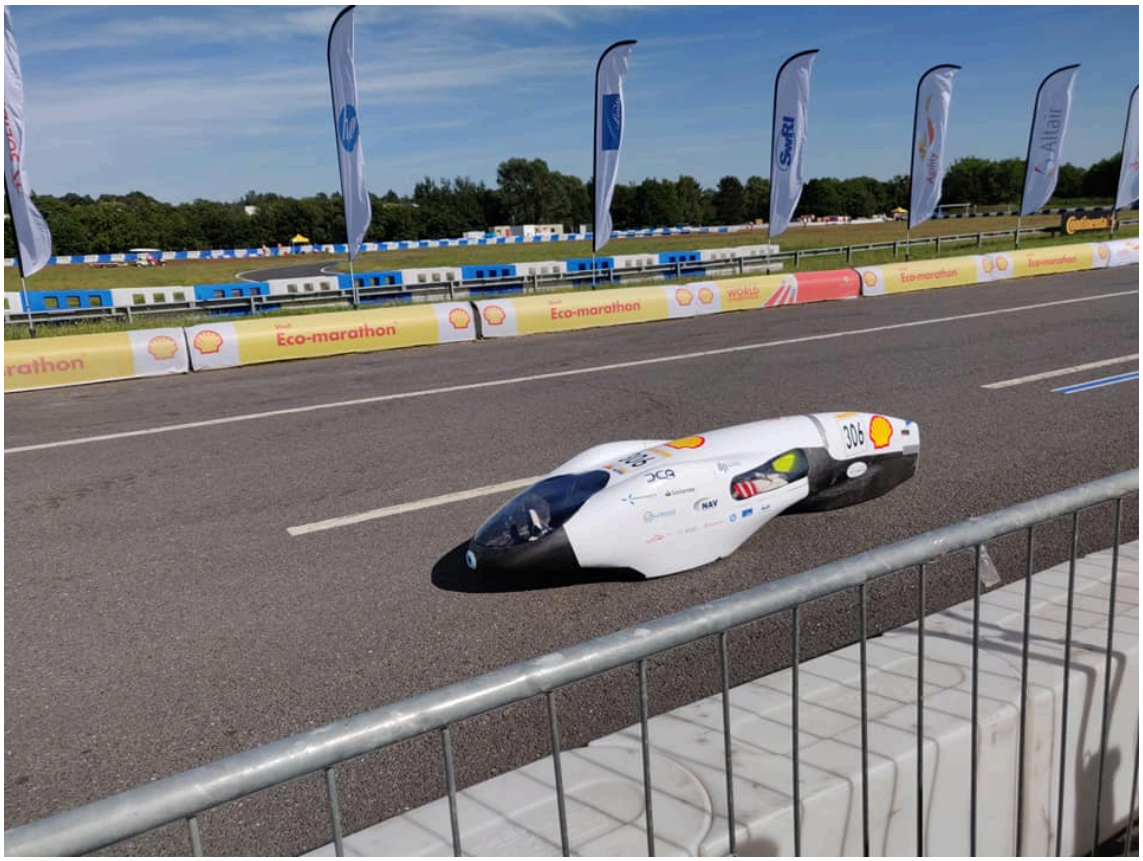

Figure 1.1: Aero@UBI 2019 Shell Eco-Marathon prototype

After a gap year, a new prototype was built, the Aero@UBI02, participating in the 2017 and 2018 editions, scoring 11th place with 371.7 km/kWh and 6th place with 519 km/kWh, respectively. Finally, in 2019 the latest and current iteration was built of the prototype was built and achieved a 612 km/kWh mark besides winning the Circular Economy Award. Unfortunately, due to the COVID-19 global pandemic the competition took an online format and suspended all track activities ever since until the present date.

1.2 Work Structure

The present work is divided into five main chapters:

- Chapter 1 gives a small introduction to the main subject and describes the SEM competition as well as the UBI's history in it.
- Chapter 2 gives a brief introduction to CFD in general, and a review of important theoretical fundamentals as well as a description of the current State of the Art.
- Chapter 3 is dedicated to describing the workflow implemented for the present study from software description and meshing setup to the final solution, as well as the hardware used to run the simulation. It also describes the entire validation using the Ahmed body to guarantee valid simulations. Lastly, describes the car's geometry, mesh and solution setup.
- Chapter 4 shows all solutions and cases related to the Aero@UBI03 Shell Eco-Marathon 2019 UBI vehicle along with all the discussion and analysis of the corresponding results.
- Chapter 5 summarizes all the important findings of this work and presents suggestions for future work.

Chapter 2

Literature Review

2.1 Fundamentals Concepts

2.1.1 Fluid Dynamics

2.1.1.1 Turbulent Flow

The external flow around a road vehicles can be either laminar or turbulent. Horner[5] describes both phenomena, firstly, the laminar flow indicates a state, where the various fluid ”sheets” that are almost parallel to the vehicle do not mix with each other, where all the stream tubes keep essentially parallel to each other and where their velocities are steady. Secondly, turbulence is a more or less irregular ”eddying” motion, a ”state of commotion and agitation”, consisting of velocity fluctuation superimposed to the main flow, within boundary layers (at higher Reynolds numbers) and within the wake behind solid bodies. Turbulent or laminar incompressible flow can be described by the Navier-Stokes Equation 2.1 and the continuity Equation 2.2:

$$\rho\frac{\partial v_i}{\partial t} + \rho\frac{\partial v_i v_j}{\partial x_j} = -\frac{\partial p}{\partial x_i} + \mu\frac{\partial^2 v_i}{\partial x_j \partial x_j} \quad (2.1)$$

$$\frac{\partial v_i}{\partial x_i} = 0 \quad (2.2)$$

The occurrence of laminar and turbulent flow depends on the non dimensional quantity known as *Reynolds Number*. This number represents the ratio between the inertial and viscous forces acting on the fluid and can be computed by the following Equation 2.3,

$$Re = \frac{U_\infty L \rho}{\mu} \quad (2.3)$$

where U_∞ is the free stream velocity, L is a characteristic length, μ is the dynamic viscosity and ρ is the fluid density.

Lastly, it is important to define the kinematic viscosity, ν. This is defined by Equation 2.4 below,

$$\nu = \frac{\mu}{\rho} \quad (2.4)$$

2.1.1.2 Computational Fluid Dynamics

In their book [6], H. K. Versteeg and W. Malalasekera, define Computational Fluid Dynamics as the analysis of systems involving fluid flow, heat transfer and associated phenomena such as chemical reactions by means of computer-based simulation. It has a wide range of industrial and non-industrial applications such as:

- Aerodynamics of aircraft and vehicles: lift and drag
- Turbomachinery
- Hydrodynamics of ships
- Meteorology: weather predictions

As such, it is an important discipline nowadays as it enables us to perform complex studies fast and with minimal costs compared to empirical experiments.
To solve fluid dynamics problems, more specifically the Navier-Stokes equations, all CFD codes use solvers that allow the use of at least one of the following techniques available:

- **Direct Numerical Simulation** — In this method, the equations are solved directly without the use of a turbulence model. It provides the most accurate results, but it needs to solve all temporal and spacial scales in detail. Hence, it requires great computational power as well as a lot of time.
- **Large Eddy Simulation** — Another, more recent method, is where the flow is characterized by eddies with a large interval of time and length scales. The largest eddies correspond to the characteristic length of the flow and the smallest ones are in charge of dissipating turbulent kinetic energy.
- **Reynolds-Averaged Navier-Stokes** — They are a time averaged equations of motion for fluid flow. The philosophy behind them is such that instantaneous quantities are split up into time averaged and fluctuating quantities as proposed by Osborn Reynolds. When the instantaneous quantities are replaced by the mean value

and corresponding fluctuation quantity (see Figure 2.1), the fluctuation variable, a set of additional equations, called a turbulence model, must be used with approximations based on knowledge of the properties of flow turbulence to give approximate time-averaged solutions to the Navier–Stokes equations. They take the form of:

$$\rho \bar{u}_j \frac{\partial \bar{u}_i}{\partial x_j} = \rho \bar{f}_i + \frac{\partial}{\partial x_j} \left[-\bar{p}\delta_{ij} + \mu \left(\frac{\partial \bar{u}_i}{\partial x_j} + \frac{\partial \bar{u}_j}{\partial x_i} \right) - \rho \overline{u'_i u'_j} \right] \quad (2.5)$$

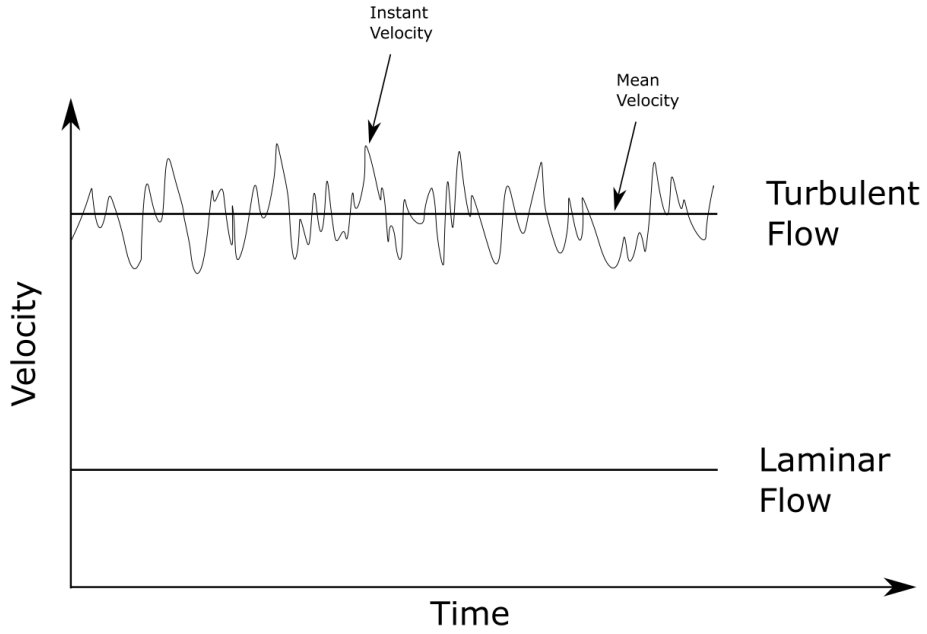

Figure 2.1: Velocities over different types of flow.

The nonlinear Reynolds stress term, $\left(-\rho \overline{u'_i u'_j}\right)$, is what requires additional modeling to close the RANS equation for solving, and thus led to the creation of many different turbulence models.

2.1.1.3 Turbulence Models

As stated before, the nonlinearity of the Navier-Stokes equations means that velocity fluctuations still appear in the RANS derivation. Thus, to obtain only the mean velocity and pressure flow field solution, a closure of the RANS equations by modeling the Reynolds stress term, as a function of mean flow, removing any reference to the fluctuating velocity.

A method was first proposed by Joseph Valetin Boussinesq by proposing relating the turbulent stresses to the mean flow. Here a new hypothesis is applied and a new constant makes its appearance, the turbulent eddy viscosity , ν_t. The hypothesis is as follows:

$$-\overline{v_i' v_j'} = \nu_t \left(\frac{\partial \overline{v_i}}{\partial x_j} + \frac{\partial \overline{v_j}}{\partial x_i} \right) - \frac{2}{3} k \delta_{ij} \quad (2.6)$$

which can be written,

$$-\overline{v_i' v_j'} = 2\nu_t S_{ij} - \frac{2}{3} k \delta_{ij} \quad (2.7)$$

where S_{ij} is the mean rate of strain tensor, ν_t is the turbulence eddy viscosity, k is the turbulent kinetic energy and δ_{ij} is the Kronecker delta.
With this new concept, turbulence models were developed over the years which helped further advance the discipline and engineering applications. Some of the models are:

- **Spalart-Allmaras (S-A)[7]** — is a one equation model that solves a transport equation for the kinematic eddy turbulence viscosity. It was strictly designed for the aeronautics ans aerospace industry as it solves wall-bounded flows and boundary layers subjected to adverse pressure gradients exceptionally well.

- $k-\varepsilon$ **(k-epsilon)[8]** — is a two equation turbulence model and one of the most common model used in CFD applications. Its original goal was to improve the mixing-length model derived by Prantl as well as finding alternative algebraical prescribing turbulent length scales in moderate to high complexity flows.

- $k-\omega$ **(k-omega)[9]** — also a common two equation turbulence model in CFD applications. The first variable being the turbulent kinetic energy and the second the turbulent specific dissipation rate, k and ω.

- $k-\omega$ **SST (Menter's Shear Stress Transport)[10]** — one of the most famous and robust turbulence model, it combines the k-omega and the k-epsilon turbulence model such that in near wall regions the former is used and in free flow regions, the latter is used.

- **Reynolds Stress equation Model (RSM)[11]** — is the most complete classical turbulence model approach. Both $k-\omega$ and $k-\varepsilon$ have shortcomings in complex

engineering solutions specially when dealing with anisotropic turbulence, recirculating flows, rotational effects and significant streamline curvature. In these flows, RSM solutions provide much better accuracy.

2.1.2 Non dimensional Coefficients

Vehicles in general are acted upon four forces (see Figure 2.2 those being drag, lift, weight and thrust. In this section we will only focus on the relevant ones for the present work, these being drag and lift.

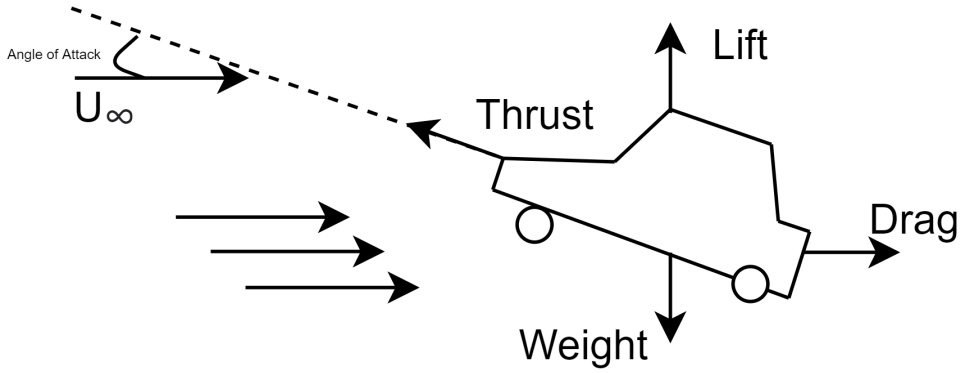

Figure 2.2: Forces diagram.

2.1.2.1 Drag Coefficient

As stated before, this is one of most important parameters in the vehicle design since it is directly tied to fuel efficiency which is an important aspect of the competition. Drag is the force that acts in the opposite direction of the movement of an object through a fluid environment such as water or air. There are two types drag: pressure and friction drag. Pressure drag is a contribution mainly due to the shape of the object, e.g. *on streamlined shapes have higher pressure drag than streamlined shapes*, and friction drag which is created by the contact of the fluid with a surface which in turn creates friction. In road vehicles pressure drag is the most relevant aspect while in airfoils friction drag takes the spotlight.

The drag coefficient is a non dimensional quantity where the drag force is divided by the dynamic pressure multiplied by the area projected in a set direction (typically the free stream direction) as seen in Equation 2.8. Since drag depends of the shape and size of the car front bodywork, one concern car designers have in mind is the reduction of the frontal area as this reduces drag. Thus, a quantity named drag area $C_D A$ is usually employed to have a more intuitive way to compare drag between vehicles since its rare to have two cars

with the same frontal area or shape.

$$C_D = \frac{D}{\frac{1}{2}\rho U_\infty^2 S_w} \quad (2.8)$$

2.1.2.2 Lift Coefficient

The lift coefficient is defined similarly to the drag coefficient, the difference being that the force is perpendicular to the motion of the body. One can compute the coefficient with the following Equation,

$$C_L = \frac{L}{\frac{1}{2}\rho U_\infty^2 S_w} \quad (2.9)$$

Lift or downforce generates a type of drag called induced drag and is defined by the drag generated whenever an object redirects incoming flow. Usually in fast moving vehicles there is a compromise between downforce and drag in order to make the car steerable at high speeds. In our case, since the desired velocity is $7m/s$ the vehicle does not need any downforce generation. Thus, the one of the main objectives is to have the vehicle angle of attack in such a way that the lift component is null and therefore the induced drag is zero.

2.1.2.3 Pressure Coefficient

The pressure coefficient is a non dimensional quantity that describes the relative pressure at any given point in a field. According to Equation 2.10 the difference between the local pressure and free stream pressure divided by the free stream dynamic pressure. Since the pressure coefficient is independent of the vehicle speed, it is much more convenient and intuitive to use than relative pressure.

$$C_P = \frac{p - p_\infty}{\frac{1}{2}\rho_\infty U_\infty^2} \quad (2.10)$$

2.1.3 Boundary Layer

As a fluid moves around an object, the fluid elements close to its surface are disturbed by the presence of the surface wall and move accordingly to it. The particles right next to it, stick to the surface and thus, have null velocity. The process creates a region of fluid near the surface in which the velocity increases from zero to the free stream value away from

the surface. This thin region attached to the object surface is referred to as the boundary layer as seen in the Figure 2.3

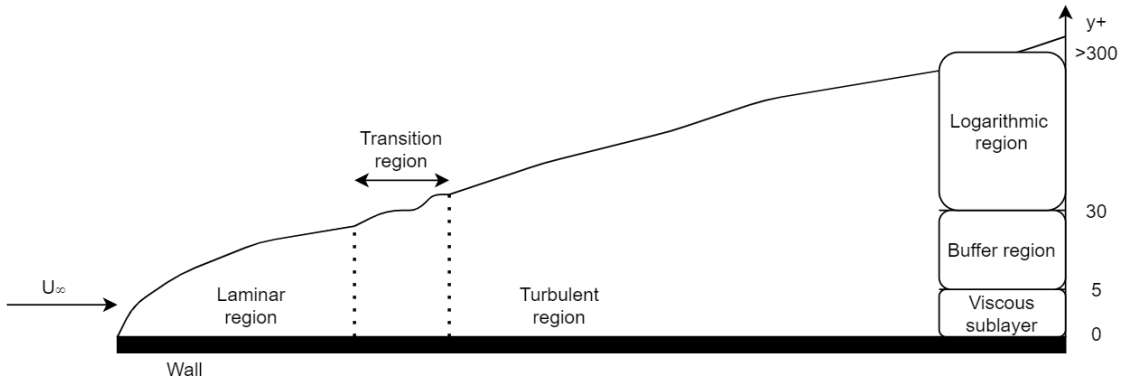

Figure 2.3: Boundary Layer representation.

The boundary layer is divided into three regions:

- Laminar region.
- Transition region.
- Turbulent region.

In the laminar region the fluid flows smoothly, as described previously (Section 2.1.1.1), like a stack of sheets of the fluid all sliding next to each other. Such, behaviour creates a shear force between the sheets which causes them to slow down. As the fluid gets further away from the wall the shear force becomes less and less prevalent eventually disappearing and the flow goes back to having its free stream velocity. Further down stream in the boundary layer, the transition region exists. This is where the flow evolves from laminar to turbulent. In this last region, the boundary layer is fully turbulent with small scale motions known as vortexes.

2.1.3.1 The near wall region

Another important concept present in the boundary layer, is the dimensionless wall distance y^+ described by Equation 2.11.

$$y^+ = \frac{u_* y}{\nu} \quad (2.11)$$

Where u_* is the friction velocity, y the distance to the wall and ν is the kinematic viscosity. Where u_* is described as,

$$u^* = \sqrt{\frac{\tau_\omega}{\rho}} \quad (2.12)$$

Thus, it is an essential parameter that helps describe the boundary layer in CFD codes by using the Law of the Wall. The Law considers the boundary layer thickness divided in three regions as seen in Figure 2.3 where U^+ is the non dimensional velocity:

- **Viscous sublayer ($y^+ < 5$)** — Near the wall region, turbulent shear stress is absent and the fluid is dominated by viscous shear. It can be defined as a thin layer and one can assume that the shear stress is constant.
- **Buffer region ($5 < y^+ < 30$)** — It is the transition between the viscosity dominated region and the turbulence dominated region. It is a region of high complexity and thus, the velocity profiles are not very well defined. Consequently, it is a region to avoid.
- **Logarithmic region ($y^+ > 30$)** — It is where the flow is dominated by turbulence stress and the velocity profile varies with a logarithmic function along the distance y.

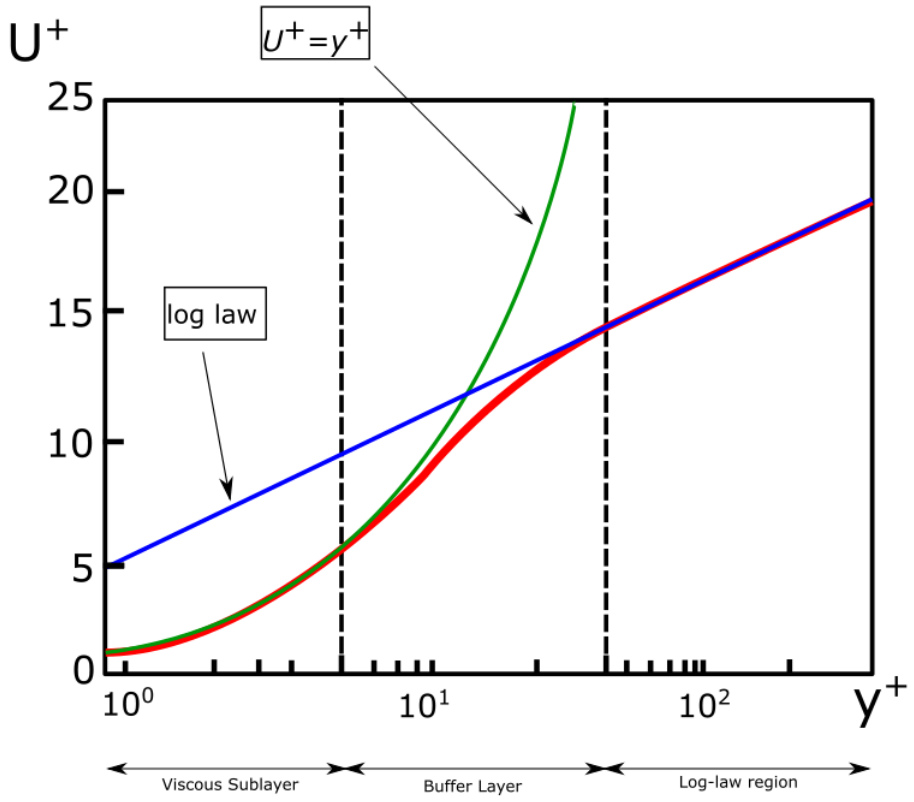

Figure 2.4: Law of the wall.

2.1.3.2 Wall Functions

In order to solve the flow in the near wall region, for example the viscous sublayer, two methods can be used. The first being to actually solve the flow all way down to the wall, by reducing the y^+ parameter of the computational mesh below 5 with suficient mesh refinement as seen in Figure 2.5. However, this method comes with a big drawback, it being the fact that one must increase the mesh resolution significantly. This leads to a finer mesh and requires more computational power, cost and time.

Another method is to use wall functions. Wall functions are empirical equations used to approximate the physics of the viscous sublayer and buffer region. These form the bridge between the wall region and the turbulent flow around the body[6]. To use this method the mesh has to be coarse ($y^+ > 30$) so that the viscous sublayer and buffer region are not resolved and wall functions can be applied, thus decreasing the amount of necessary computational power. However, wall functions do not behave very well in the case of large pressure gradients and separation. In recent years, wall functions have been designed to be capable of handling more and more adverse situations. The typical CFD software has a extensive list of wall functions that can be used to suite different needs[12].

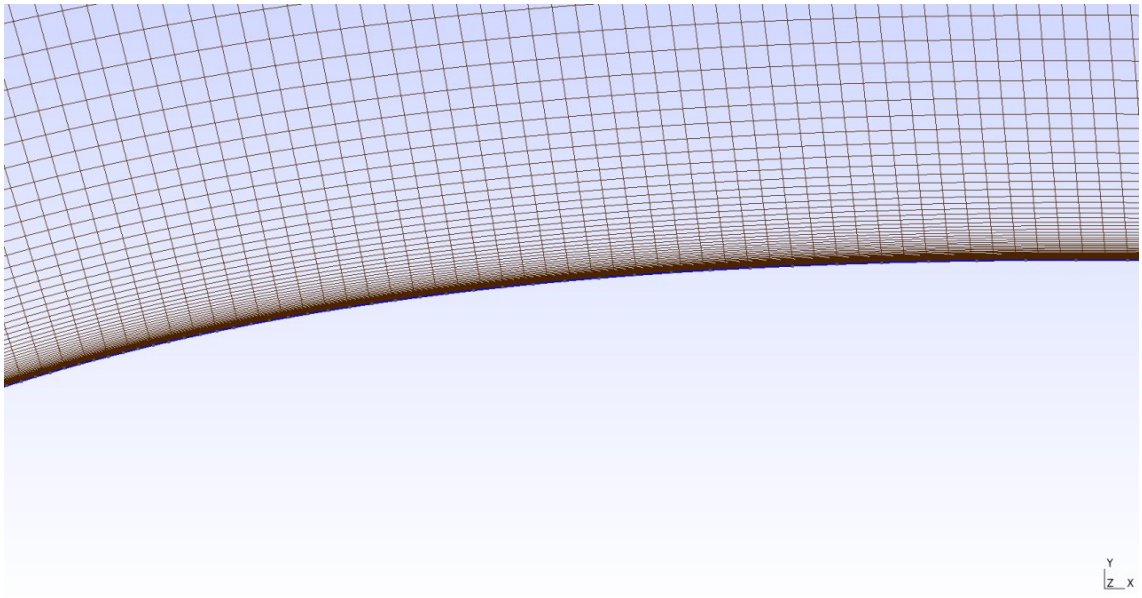

Figure 2.5: Example of a fine mesh ($y^+ < 1$).

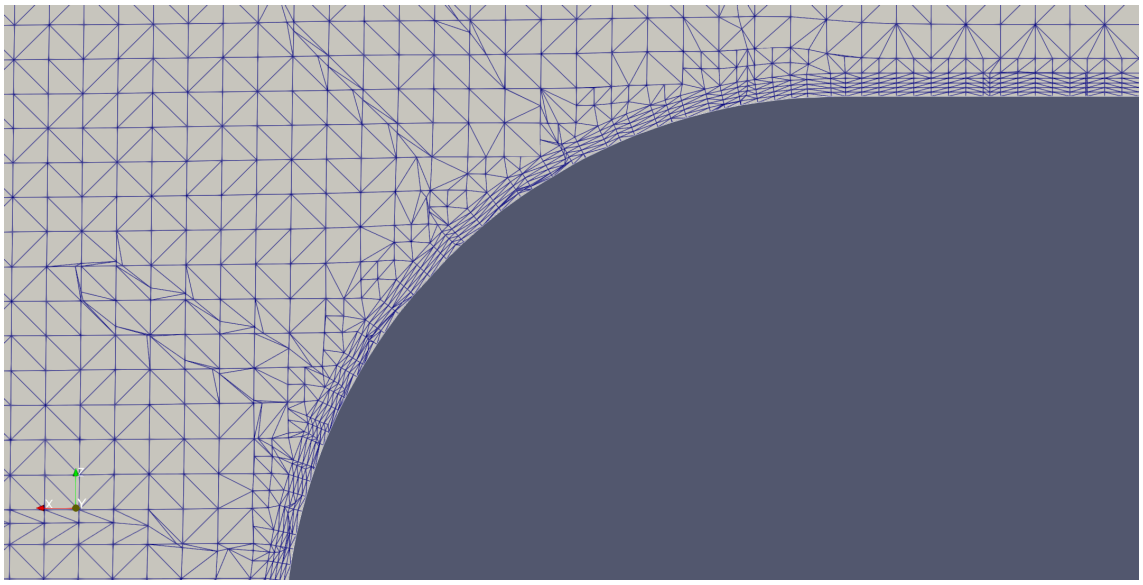

Figure 2.6: Example of a coarse mesh ($y^+ > 40$).

As a last remark, a lot of literature refers to wall functions as automatic, this is because of the method they are typically in use in current CFD software packages.. Most of the time the mesh does not have a static y^+ value over the geometry. This value can range from a small or large interval, and where the y^+ is below a certain threshold, the CFD code usually solves the flow using the first method described above. Above this threshold, depending on the wall function implementation, the wall function makes its appearance and is responsible for modelling the flow near the wall.

2.2 State of the art

In this section a short summary over the current literate regarding Shell Eco-Marathon aerodynamics and body drag literature is presented.

As stated before in Chapter 1, a previous similar study has already been done in the UBI team regarding the Aero@UBI01 vehicle in 2015[1]. Although the work focused on the design of a capable prototype, the author also provides an aerodynamic study of the vehicle design using the commercial software *FLUENT* and compares it to a similar body of revolution. As expected, the body of revolution has smaller drag coefficient, $C_D = 0.06248$, due to its lower frontal and wetted area and the uniform streamlined geometry versus the prototype's $C_D = 0.08224$. Another important result, was the discovery of separation near the final regions of both the body of revolution and the vehicle due to the existence of ground. Lastly, a study involving ground effect and the angle of attack is conducted where in the former, the values of C_D and C_L decrease due to the attenuation of the ground effect and in the latter, the same behaviour occurs due to the geometry of the vehicle thus, when a negative angle of attack is applied, the frontal area of the vehicle also decreases and reduces both coefficients[1].

Figure 2.7: AERO@UBI01 Prototype at the Eco-Shell Marathon 2015 edition[1].

In another study, E. Abo-Serie et al.[13] investigates the aerodynamic drag of a Shell Eco-Marathon prototype using the software *STARCCM+* and employing the k-ε turbulence model. The work provides an initial simulation to the vehicle after a mesh independence study and draws conclusions from it. By doing so, it later refines the vehicle design several

times improving massively the prototype overall performance from $C_D = 0.430$ up to $C_D = 0.127$.

Another work by students in the Lodz University of Technology[2], focuses on optimizing the body shape for a prototype to be used in the competition. They start by comparing their own vehicle, the Eco-Arrow, against some designs inspired by winning prototypes and evaluate speeds from $20km/h$ to $45km/h$. From their work, it is concluded that, wheels separated from the main body are not ideal as they have the highest SC_D of the entire study. Latter, both other options provide lower drag area than their current vehicle mostly due to the smaller frontal area. Between these two suggestions one stands out as, although it has the bigger frontal area, its fairings act positively and help reduce the drag coefficient.

Figure 2.8: Iron Warriors Eco Arrow 2.1[2].

Chapter 3

Methodology

This section focuses on the overall methodology used in this work.

3.1 OpenFOAM

OpenFOAM is an open source software for CFD which is maintained by several companies and a large user community. This software is essentially a C++ library composed of two kinds of applications: solvers and utilities. Solvers are made to solve a specific problem in continuum mechanics and the utilities involve data manipulation. Since it is open source, with some programming and physics background, anyone can propose and add new features to the software. Along with the CFD capabilities, *OpenFOAM* comes with pre- and post-processing environments[14].
An important aspect of this software is that it does not possesses a GUI, thus a lot of companies focus in providing one. An extensive list can be found in [15]. In order to be considered, the application would have to pass a few requirements such as: documentation available, open source and previous user experience. As such, the *HELYX-OS* was chosen since there are a plethora of tutorial presentations as well and many students and teachers had already used it in our university. However, one of the main *HELYX-OS's* shortcomings is its lack of support regarding the more recent versions of *OpenFOAM* which in turn led to many of the available options not show up on the GUI and had to be manually inserted just as a normal user would without *HELYX-OS*.

3.1.1 *k*-ω *SST*

The *k*-ω *SST* turbulence model was developed by Menter[10]. This particular model uses the *k*-ω turbulence model for predicting the boundary layer and the *k*-ε model to predict the external flow far from the wall. To achieve this, the model uses a blending function based on the distance from the wall to determine the weights of each model, additionally it also aims to overcome the deficiencies of the k-ω model. Since its introduction in 1994 the model has been validated by countless authors and it has proven to be a robust and reliable model.

The turbulence boundary conditions are calculated based on the *OpenFOAM's* implementation of the model, hence[16]:

$$k = \frac{3}{2}\left(I\left|U_\infty\right|\right)^2 \quad (3.1) \qquad\qquad \omega = \frac{k^{0.5}}{C_\mu^{0.25} l} \quad (3.2)$$

3.1.2 Convergence

In CFD, determining if a solution has converged is usually a difficult process. Most of the times, solutions can be considered converged if the flow field does not change over time, however, in unsteady flows this is not the case. Nevertheless, convergence can occur at different criteria. One of these criteria is called *Residual*, they are the differences in the values of a quantity between two iterations. Thus, the more the residuals are low the fewer changes it will occur to the solution as the iterations continue. Every CFD software has its own way of implementing this concept. It is also normal to provide a converged flow solution criterion value, in essence, what this means is that when the residual goes below a certain criterion, the simulation has converged. One thing to note is that, low residuals do not automatically mean a correct solution, and high residuals do not automatically mean a wrong solution since there could be a number of flow structures that do not let the residuals fall below the established criterion value. Thus, another important aspect of convergence is monitoring a physical quantity. Since the goal is to predict forces, they will also be used as a criterion for convergence.
In this present work, convergence is assumed when the residuals meet the established 10^{-5} criterion and the forces (SC_D and SC_L) show a periodic behavior or the residuals and forces show a periodic behaviour.

3.2 SnappyHexMesh

For meshing purposes, the *OpenFOAM's BlockMesh* and *SnappyHexMesh* utilities were used. While *BlockMesh* is used to create the initial mesh, *SnappyHexMesh* is used to iterate over that base mesh while adding user defined features to improve and sculpt the mesh to the user demands. Both of these utilities use the simple *OpenFOAM* file format and with the abundance of documentation available, one is able can create a mesh suited for any need while having full control over its parameters.

3.2.1 Refinement Level

For refining purposes, *SnappyHexMesh* takes the base mesh cell size and does its refinement in form of levels. This process uses equation 3.3 as its driving mechanism. Coupled together with *SnappyHexMesh* versatility we can define sections and areas of the domain with different refinement levels in order to capture the flow details more accurately.

$$RefinedCellSize = \frac{BaseMeshCellSize}{2^{RefinementLevel}} \quad (3.3)$$

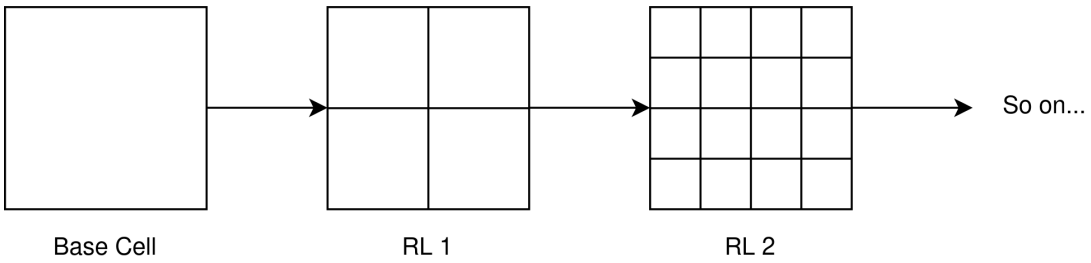

Figure 3.1: Refinement of the mesh with each level.

3.2.2 surfaceFeatureExtract

Another tool used for mesh creation was the *surfaceFeatureExtract* utility. This utility was used to extract the lines of the STL into a .eMesh file which can be used by *SnappyHexMesh*. It allows the STL to have greater refinement and detail. In the body refinement section - table 3.3 - it is referred as *line* followed by the level of refinement.

3.2.3 Mesh Quality

Finally, the mesh had to go through the *checkMesh* utility before being used for any simulation. The utility compares the mesh features against a list of mesh quality constraints that can be user defined or defaulted by the software. If the mesh passes the check it is ready for simulation.

However if its quality is not up to par by default all cells that do not comply with the mesh quality constraints get written into separate files. The creation of these files allows us to group all the cells together into one file using the *topoSet* utility and then generate a new mesh without the bad cells (see Figure 3.2. This is done by inverting the set containing the bad cells using the *setSet* utility, thus generating all the good cells into a file. Then using the *subsetMesh* utility, one can generate a mesh with the good cells. The process creates

a new boundary named *oldInternalFaces* set by default to empty which in turn is set to symmetry in order not to affect the final solution significantly.

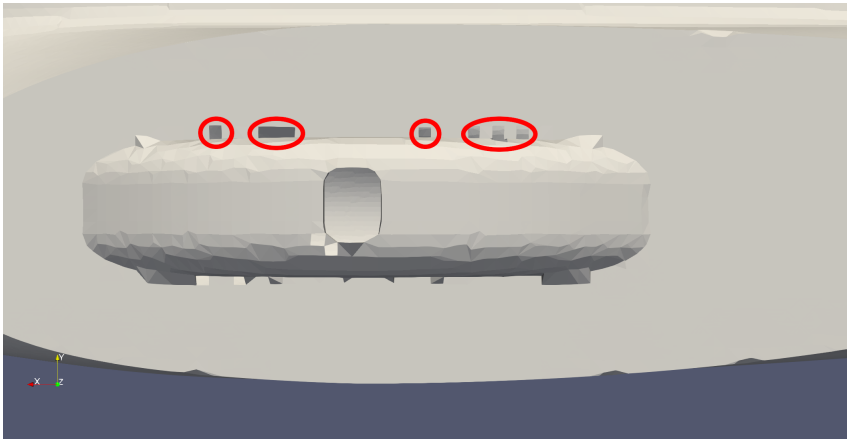

Figure 3.2: Example of removed cells.

3.3 *ParaView*

For post processing analysis, the software *ParaView* as used. It is an open-source, multi-platform data analysis and visualization application for CFD data post-processing. Users can quickly build visualizations to analyze their data using qualitative and quantitative techniques. The data exploration can be done interactively in 3D or programmatically using ParaView's batch processing capabilities. It was developed to analyze extremely large datasets using distributed memory computing resources. It can be run on supercomputers to analyze datasets of petascale size as well as on laptops for smaller data, has become an integral tool in many national laboratories, universities and industry, and has won several awards related to high performance computation[17].

3.4 Simulation Setup

For the present work, the creation of a streamlined workflow helped immensely by reducing the amount of work necessary to setup the simulations and the time between each simulation. Consequently, the work was efficient and only bottlenecked by computational power. All the cases followed the same workflow, only having small differences for each geometry. Figure 3.3 shows the general workflow of the obtaining a flowfield solution for a new vehicle geometry or computational mesh.

The software *HELYX-OS* was extensively used. Its purpose was to generate all the case files, as opposed having to copy and edit one of the *OpenFOAM's* tutorials. Along side with

this, it was used to help with the initial mesh setup thanks to its aforementioned GUI.

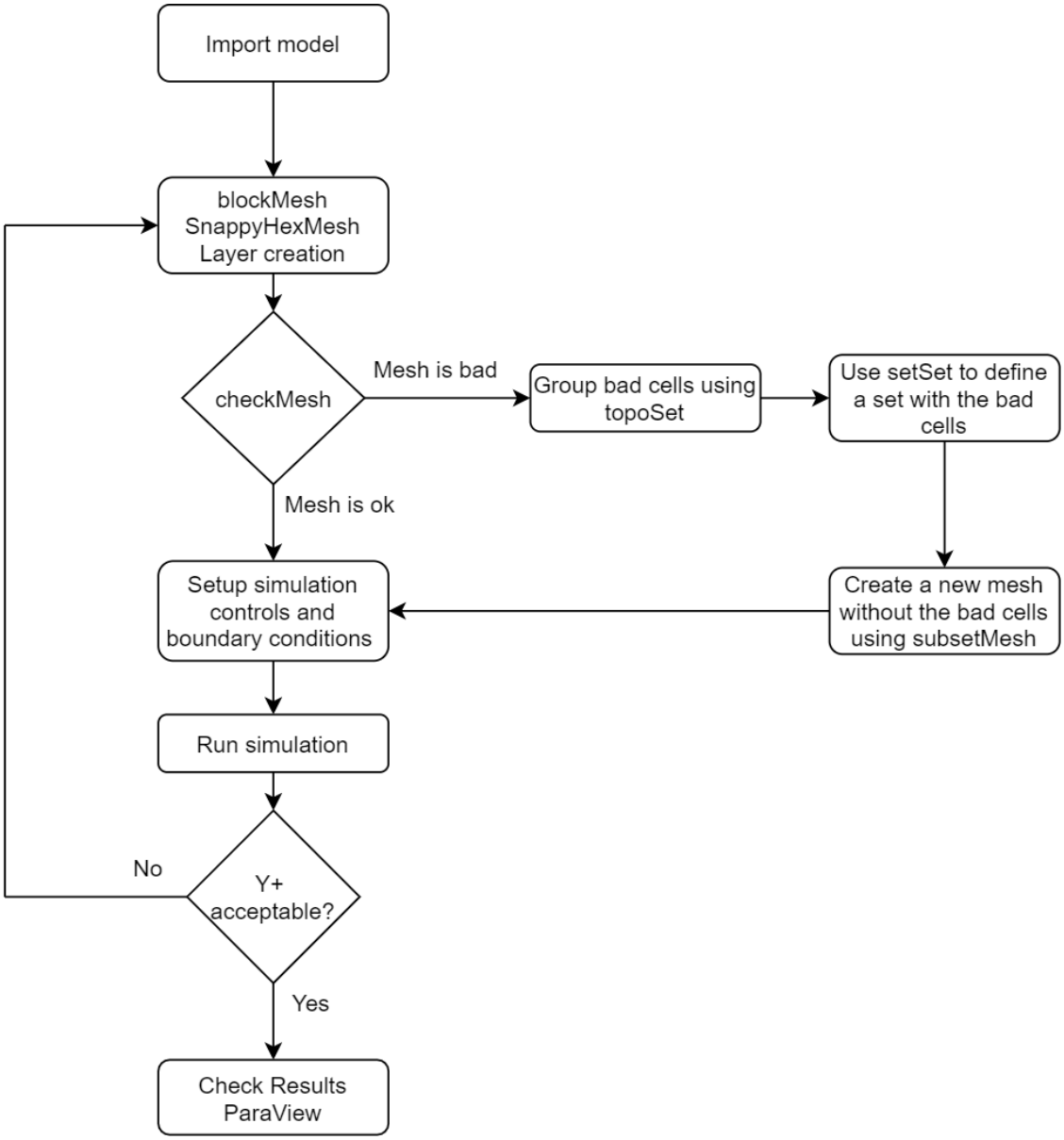

Figure 3.3: Simulation workflow.

The work begins by importing the relevant vehicle geometry STL file into the *OpenFOAM* case, where depending on its data, needs to be resized to millimeters. Secondly, the domain and the *SnappyHexMesh* parameters are set and an initial mesh is created. This mesh goes through the *checkMesh* utility where, depending on the result, it suffers different treatments. If the mesh is suited for simulation, the next step in the workflow can be taken, else if the mesh is not up to par to the quality constraints, the process explained in Subchapter 3.2.3 is executed. With the mesh ready for simulation, the simulation run time and all other parameters (Velocity magnitude, pressure, e.g.) are set up. Lastly, the simulation is ran until a convergence is reached and using the post processing utility *yPlus* one

can make an assessment if the y^+ is acceptable. If its not, the whole process is repeated, else results are checked using the post process software *ParaView*[17].

3.4.1 Meshing setup

As described in Chapter 2, the first step is to define the domain. This is done in function of the vehicle overall length, L, and done in way not to create the blockage effect. This effect arises when the streamlines surrounding the body are effect by the walls of the domain. This effect is calculated by measuring the ratio between the body frontal area and the domain cross section as seen in Equation 3.4. According to [18], a blockage factor <3% is recommended for good results, to which the present work has 0.88%.

$$\text{Blockage factor} = \frac{\text{Body frontal area}}{\text{Domain cross section}} \quad (3.4)$$

The domain consists of a rectangle with $9L \times 4L \times 3L$ dimensions as shown in Figure 3.4. The wake region, from the vehicle to the downstream outlet domain boundary, twice as long as the upstream distance from the vehicle to the inlet, for the purpose of capturing the wake effects and their development.

With the initial boundaries defined, it is necessary to setup the second part of the meshing procedure using *SnappyHexMesh*. With the *HELYX-OS* software, two new refinement regions are created (See Figure 3.5). The first region, a rectangular box, close and around the vehicle, is used to refine the mesh around the vehicle, where the strong flow parameters gradients exist, for more accurate flow simulation results such as separation and stream lines. The second region, similar to the first region, is used as a transition refinement area between the first box and the overall domain. Next, is defining the number layers for the vehicle surface wall boundary layer simulation. Two distinct methods were used to create layers on the Ahmed body and Shell Eco-Marathon 2019 car. This is due to the first method, used in the Ahmed body, did not yield good results when implemented on the Shell Eco-Marathon vehicle. Hence a second method had to be devised.

The first method, made use of the layer software already implemented in *SnappyHexMesh*. Thus, with the first mesh point target y^+ of 40 in mind, a lot of trial and error runs were performed to derive a good set of parameters. The three mesh layering control variables used were: *nSurfaceLayers*, *expansionRatio* and *firstLayerThickness*. Firstly, using a flat plate as reference, an initial guess was obtained. After that, a careful study was made, changing each criteria one at a time in order to understand each one's influence on the y^+.

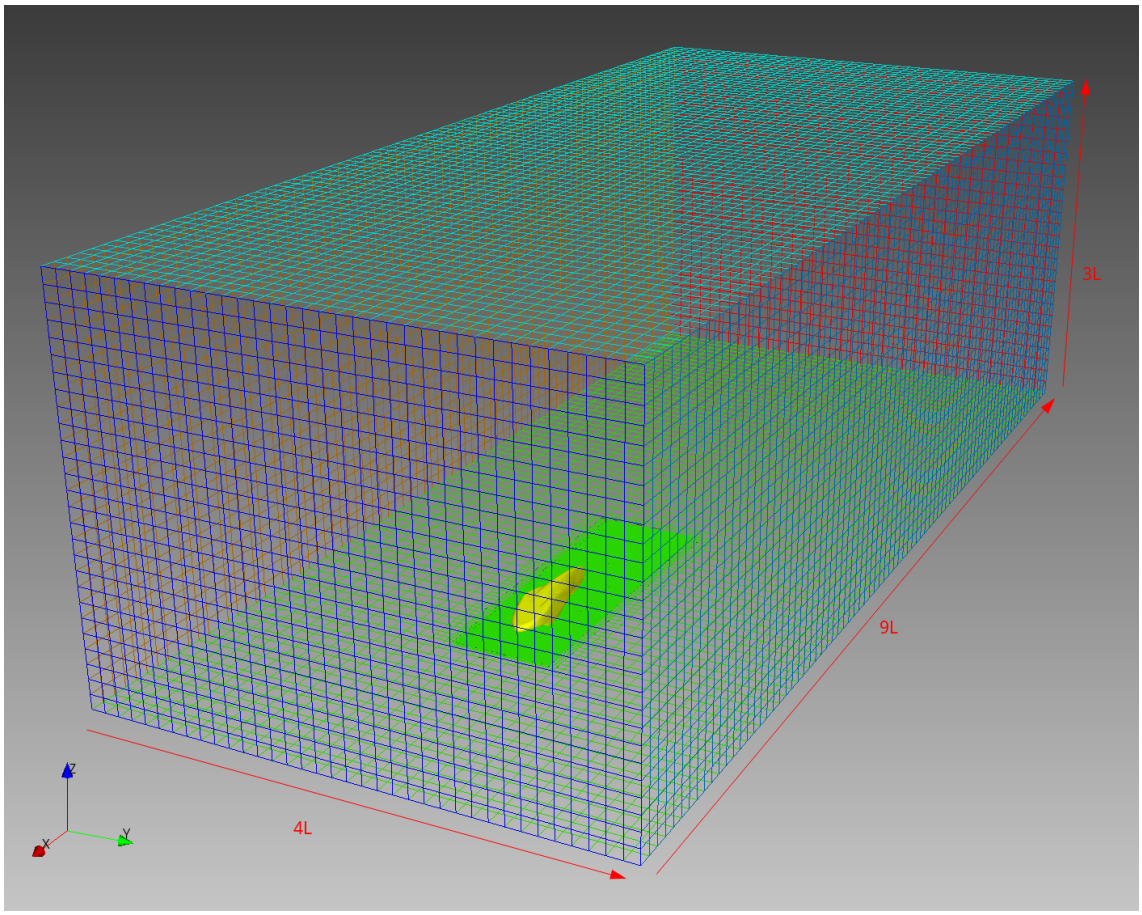

Figure 3.4: Simulation Domain (L is the vehicle length).

The second method, also relied on the capabilities of *SnappyHexMesh*, however unlike the first method, an additional treatment had to be done in order to create a suitable mesh. First of all, a single large layer was created using *SnappyHexMesh*, based on the previous testing done with the Ahmed body flow simulations. Secondly, using the utility *refineWallLayer* four more layers were created manually. The end result was a layer region with a the first mesh point at y^+ of 40, however the generated mesh did not pass the quality checks imposed by the *checkMesh* utility. A solution was then obtained by using the procedure described in section 3.2.3.

3.4.2 Solution Setup

After the meshing process is complete, one must define the boundary conditions present in the *0* folder. In this folder, all the quantities relative to the turbulence model are found - kinetic turbulent energy , turbulent viscosity, specific turbulence dissipation rate , velocity and pressure - and their respective value. It is important to refer that the standard wall functions of wall functions was not used most of the time. Instead a different set were

used, this is because since, although the average y^+ is 40 in both cases, both had sections where the y^+ ranged from 0 to 300, hence a more smooth approach was desired. For the specific turbulence dissipation rate, the *binomial2 blending (continuous)* method was used. This estimation is blended between the viscous and inertial sublayer estimations by using a binomial[19] function as seen in Equation 3.5,

$$\omega = \left((\omega_{vis})^2 + (\omega_{\log})^2 \right)^{1/2} \quad (3.5)$$

As for the turbulent viscosity, the *nutUSpaldingWallFunction* was employed. The wall function has the following properties[20],

- The *nutUSpaldingWallFunction* boundary condition provides a wall constraint on the turbulent viscosity, i.e. ν_t, based on velocity, i.e. U for low- and high-Reynolds number turbulence models
- Using Spalding's law gives a continuous ν_t profile to the wall

Lastly, in this topic, the standard kinetic turbulent energy wall function was used[21]. Secondly, the turbulence models and fluid properties were defined in the *constant* folder. For this work, the fluid air was used with the properties of Table 3.1.

Table 3.1: Fluid properties.

Properties	
ρ (rho)	1.225 kg/m^3
μ (mu)	1.825E-5 kg/(m.s)
ν (nu)	1.489E-5 m^2/s

Lastly, the *system* folder is addressed. Here the file *controlDict* sets the controls for the simulation, such as number of time steps, the time step size and how the results are writ-

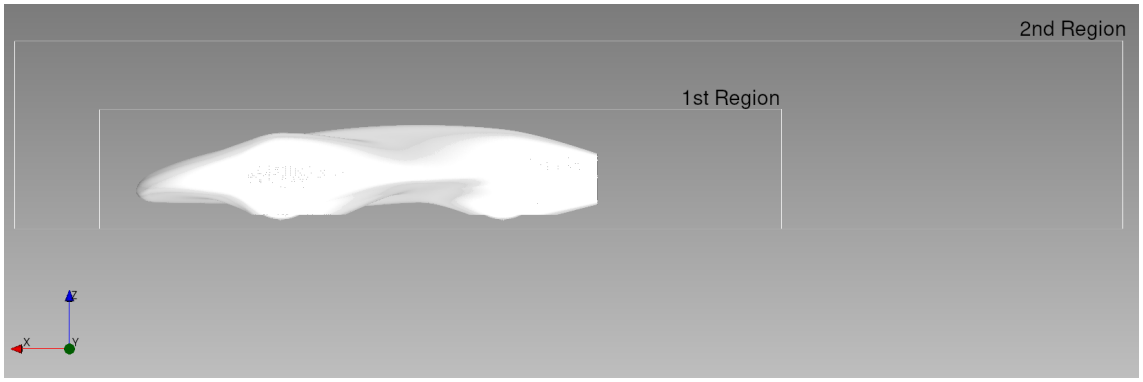

Figure 3.5: First region and second refinement region.

ten. One can also include functions such as the calculation of forces and moments on certain patches and many other.

With all the settings set, the simulation can now be performed. Due to the computational resources required to run simulations, *OpenFOAM* provides a way to parallelize the case in hand using the *Open MPI* software. This allows the case to run on multiple cores of the CPU, accelerating the result. *OpenFOAM* provides a utility, *decomposePar* which takes its settings from a file named *decomposeParDict* placed inside the *system* folder to decompose cases into a parallel affair. After the case has been decomposed and ran, because the results are scattered through multiple processors and, in order to view and process them, the case must be reconstructed using *reconstructPar*.

The numerical methods were also defined in the file *fvSchemes*. The chosen methods were:

Table 3.2: Numerical divergence schemes.

Quantity	Scheme
U	Gauss linearUpwindV cellMDLimited Gauss linear 1
k	Gauss linearUpwind cellMDLimited Gauss linear 1
ω (Omega)	Gauss linearUpwind cellMDLimited Gauss linear 1
ν_t (nut)	Gauss linearUpwind cellMDLimited Gauss linear 1

Firstly, the *Gauss* entry specifies the standard finite volume discretisation of Gaussian integration which requires the interpolation of values from cell centres to face centres. The interpolation scheme is then given by the *linear* entry, meaning linear interpolation or central differencing. Secondly, the keyword *linearUpwind* refers to a second order, upwind-biased, unbounded, that requires discretisation of the velocity gradient to be specified. This can be complemented by the *'V'* letter changing the method to a *V-scheme*. *V-schemes* are specialised versions of schemes designed for vector fields. They differ from conventional schemes by calculating a single limiter which is applied to all components of the vectors, rather than calculating separate limiters for each component of the vector[22]. The *V-schemes'* single limiter is calculated based on the direction of most rapidly changing gradient, resulting in the strongest limiter being calculated which is most stable but arguably less accurate. Thirdly, to specify the gradient scheme, a less diffusive, more accurate solution and more unstable using *cellMDLimited Gauss linear 1* was used. In summary, using the second order *linearUpwind* we assure a stable solution and with *cellMDLimited Gauss linear 1* a more accurate solution.

Post processing was made using the third party *ParaView* software and the post processing utilities build into *OpenFOAM*.

3.4.3 Hardware

For this simulation a desktop personal computer containing an AMD Ryzen 5 2600 Hexa-core processor at 3.6 GHz and 16GB CL14 3200MHz DDR4 memory were used. The simulations ran using all of the 12 threads available and, in the mesh 4 case (see Table 3.3 for its characteristics) used all of the RAM and most memory from the Linux swap partition (8GB). Consequently, with such high memory usage, it was concluded that meshes finer than mesh 4 were out of reach for the available computational resources.

3.5 Validation

In this chapter, the validation process will be discussed. This is an essential part of the work as it validates the methodology described in Chapter 3.

3.5.1 Ahmed Body

Created by Ahmed in 1984[4], the Ahmed body captures the most important flow features present in road vehicles. The body, as seen in Figure 3.6 consists of a generic simple shape such that it was capable of generating a tree-dimensional displacement flow in the front, relatively uniform flow in the middle, and a large structured wake at the rear. It quickly became an industry standard in validation, thanks to its simplicity and empirical experiments conducted by Ahmed and other authors.

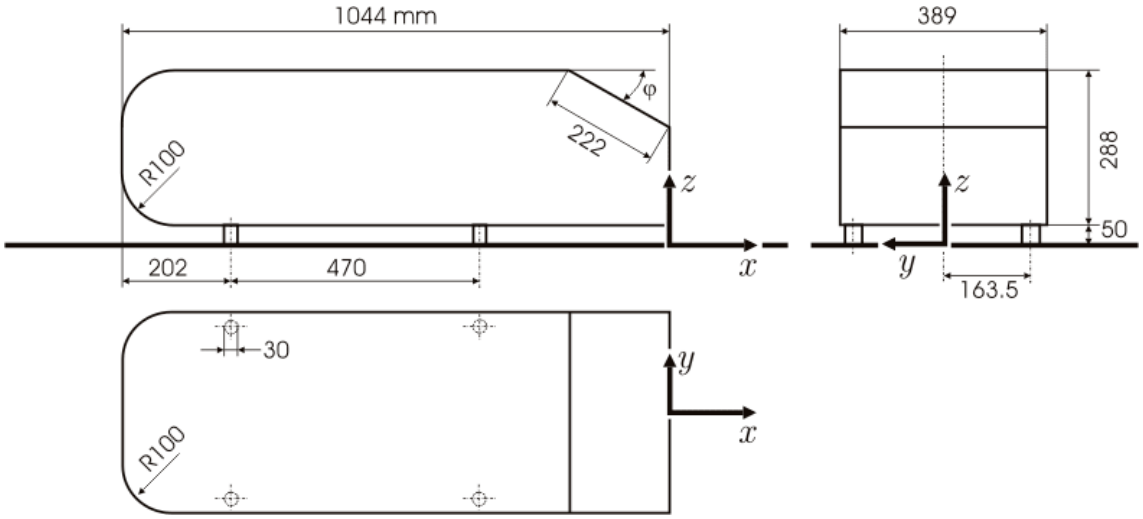

Figure 3.6: Ahmed body specifications[3]

In his work, Ahmed tested for several slant angles and showed that the wake was comprised of four distinct structures as shown in Figure 3.7.

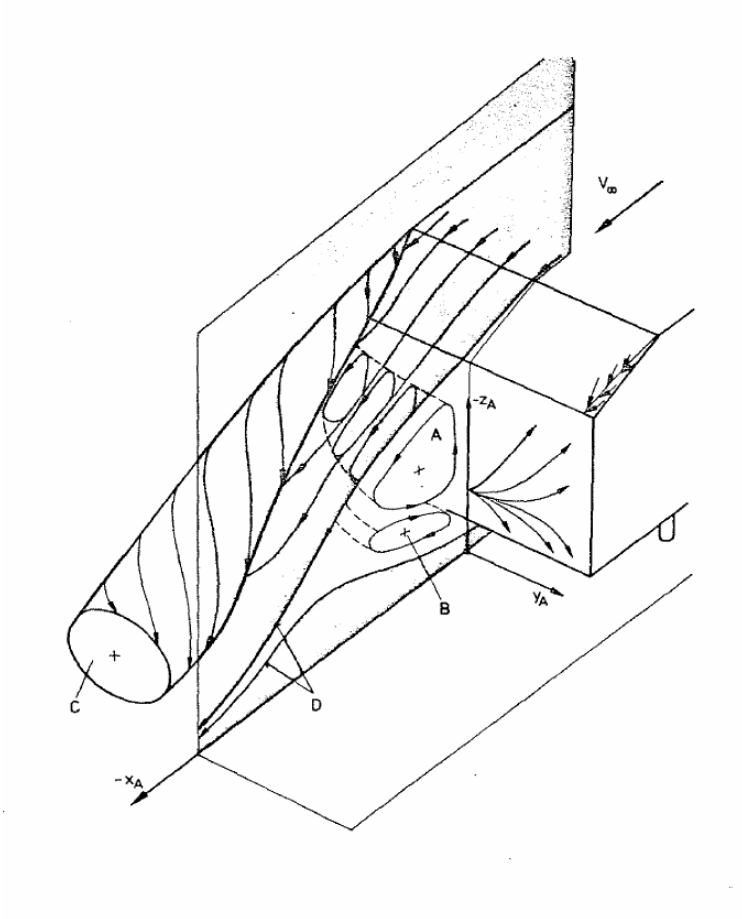

(A) Recirculatory region coming of the slant region.

(B) Recirculatory region coming from the underbody.

(C) Pillar Vortex coming of the slant side edge.

(D) Separation bubble boundary.

Figure 3.7: Vortex system in wake schematic[4]

In conclusion, the wake was shown to be highly dependent on slant angles. For a slant angle of less than 12°, the flow remains attached over the slant. The flow is essentially two-dimensional and has low drag. Between 12° and 30° the flow becomes much more three-dimensional as the C-pillar vortices form. These reach maximum strength at 30°. The drag increases significantly as the low pressure cores of these vortices act on the rear surfaces. Past 30° the flow separates fully off the slant. This results in a sudden decrease in drag and weaker c-pillar vortices[3].

In his work, Ahmed analyses the drag created by the body at various slant angles creating a schematic for such. Another result of his experiment is the cross flow velocity at various stations downstream of the wake.The drag analysis and more detailed wake schematics can be found in the original article[4].

In the present work, as the validation case of the numerical study setup, work, a 25°slant angle will be used since there's a lot of literature regarding this specific case, making it easier to evaluate the validation results.

As for the validation procedure, table 3.3 presents all the meshes and their characteristics

that were analysed during this process.

Table 3.3: Mesh characteristics.

Mesh	Cell Size			Body Refinement		Layers		Mesh Statistics		
1	X	Y	Z	Ahmed	4 4 + line 4	N Layers	5	Points	Cells	Faces
	0,2	0,199	0,196	Box	3	Expansion ratio	1,05	236997	213867	664525
				Box 2	2	1st layer thickness	0,00087			
2	X	Y	Z	Ahmed	5 5 + line 5	N Layers	5	Points	Cells	Faces
	0,2	0,199	0,196	Box	4	Expansion ratio	1,05	1469920	1386178	4241884
				Box 2	3	1st layer thickness	0,00087			
3	X	Y	Z	Ahmed	6 6 + line 6	N Layers	5	Points	Cells	Faces
	0,2	0,199	0,196	Box	5	Expansion ratio	1,05	4810412	4567714	13945283
				Box 2	3	1st layer thickness	0,00087			
4	X	Y	Z	Ahmed	6 6 + line 6	N Layers	5	Points	Cells	Faces
	0,2	0,199	0,196	Box	5	Expansion ratio	1,05	10025677	9705630	29436171
				Box 2	4	1st layer thickness	0,00087			

3.5.2 Boundary conditions

The general boundary conditions go as follows:

- Inlet velocity 40 m/s
- Pressure outlet set to 0 Pa
- Ground velocity set to 40 m/s
- Symmetry conditions on the side and top boundaries

For the turbulent boundary conditions, using Equations 3.1 and 3.2 the values in table 3.4 were set,

Table 3.4: Turbulent boundary conditions.

Freestream Velocity (U_∞)	40 m/s
Turbulent Intensity (I)	1%
Turbulent kinetic Energy (k)	0.24
Turbulent Length scale (l)	0.47 m
C_μ	0.09
Specific rate of dissipation (ω)	1.96

Both turbulent intensity and length scale were assigned according to [23] and [24], where the latter is the vehicle wheelbase which is representative of the size of the largest eddy.

3.5.3 Validation Results

In this section, the present results for the simulation of the wake structures and the cross flow velocity downstream of the Ahmed body are inittially evaluated. In addition , to com-

plete the numerical procedure validation, the drag coefficients are compared. Finally, a few remarks regarding the simulation y_+ and run time are discussed.

3.5.3.1 Wake structure

As described in Subsection 3.5.1 , the important flow regions of the Ahmed 25° slant angle body flow are correctly predicted by the present simulation as seen in figure 3.8. Regions A and B are shown in Figure 3.8a while vortex C is shown in Figure 3.8b. Region D can be found more explicitly in Figures 3.8a and 3.8c.

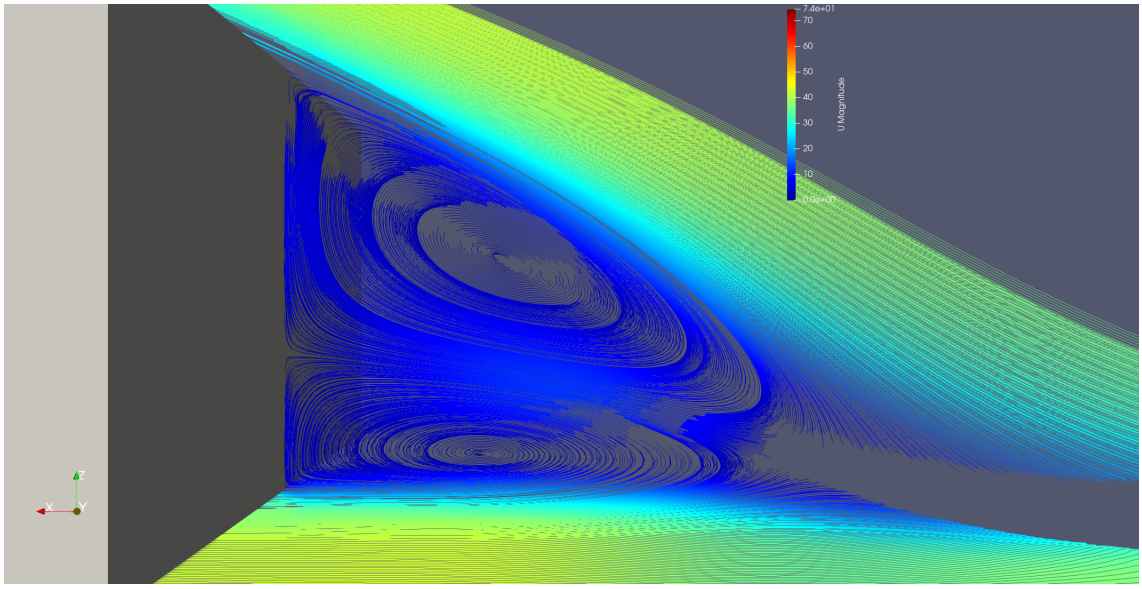

(a) Recirculatory regions A and B.

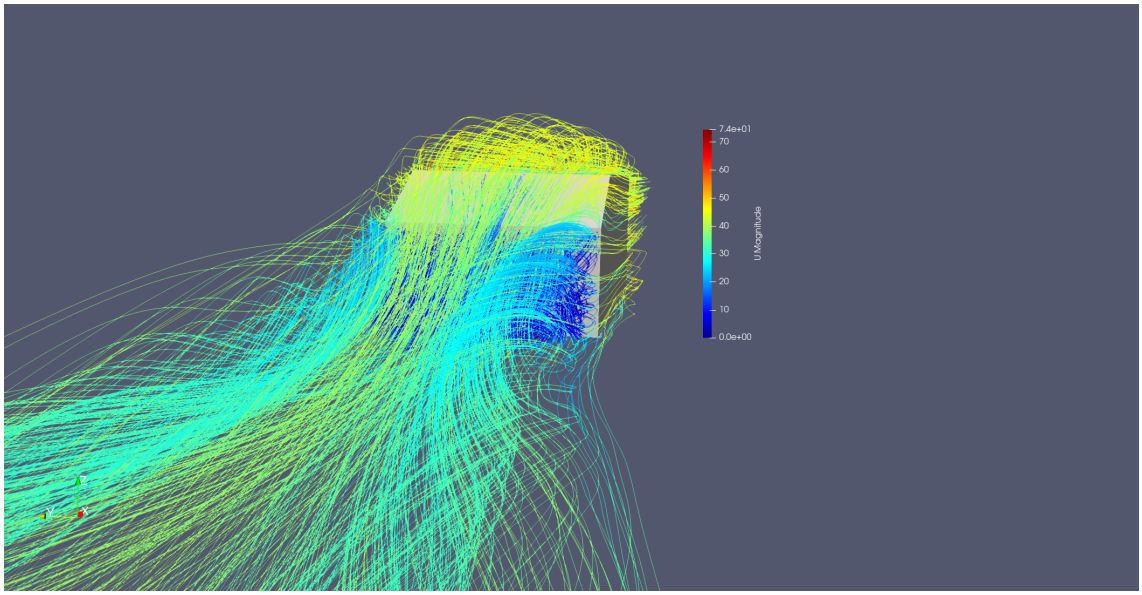

(b) Vortex C.

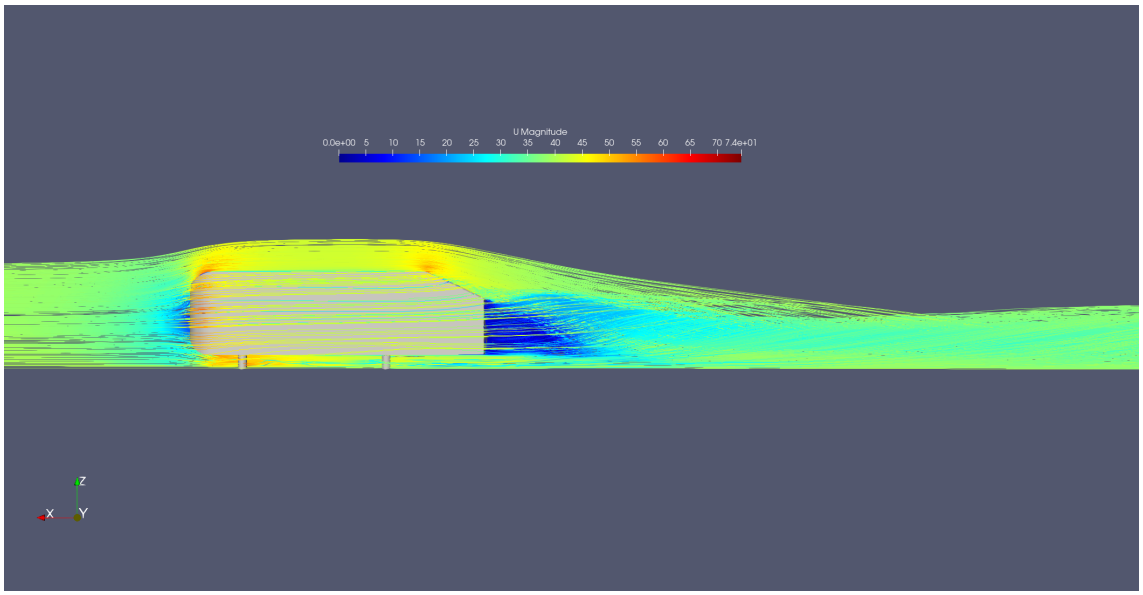

(c) Side view of the flow.

Figure 3.8: Simulated Ahmed 25° slant angle wake mean flow trace lines and U velocity component magnitude (Mesh 3).

In addition to the wake structure, Ahmed[4] examines the cross-flow velocity distribution at three downstream positions, in order to evaluate the flow along the wake. These positions are located at $x_a/l = -0.077, -0.190, -0.479$ where x_a is the x coordinate with respect to the frame of reference shown in Figure 3.6 and l is the body length . The Figures 3.9, 3.10 and 3.11 make the comparison between the experimental and present CFD results.

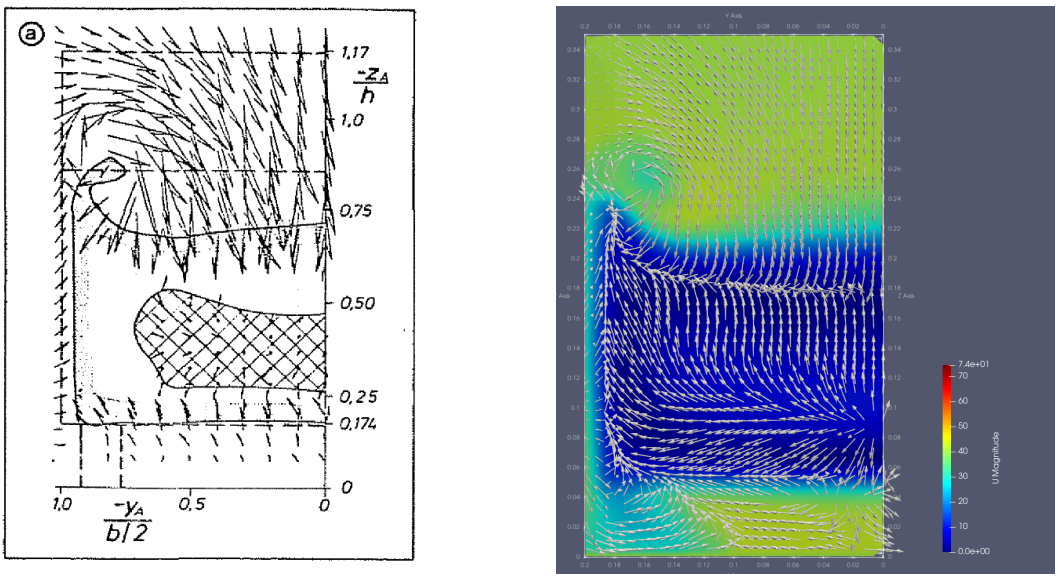

Figure 3.9: Mean flow velocity vector field and U velocity component magnitude at $x_a/l = -0.077$ (mesh 3).

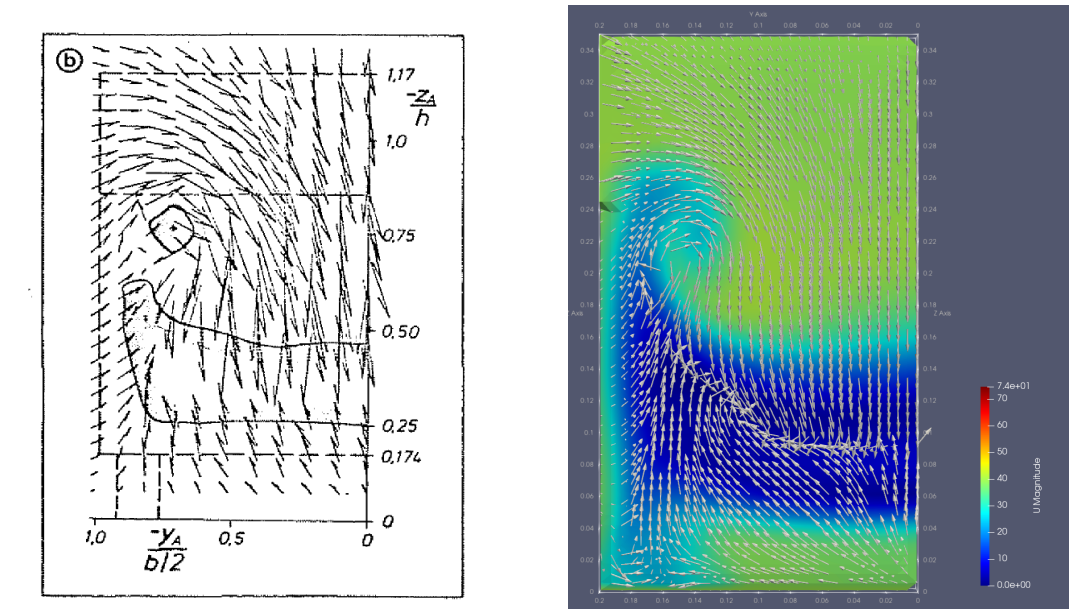

Figure 3.10: Mean flow velocity vector field and U velocity component magnitude at $x_a/l = -0.190$ (mesh 3).

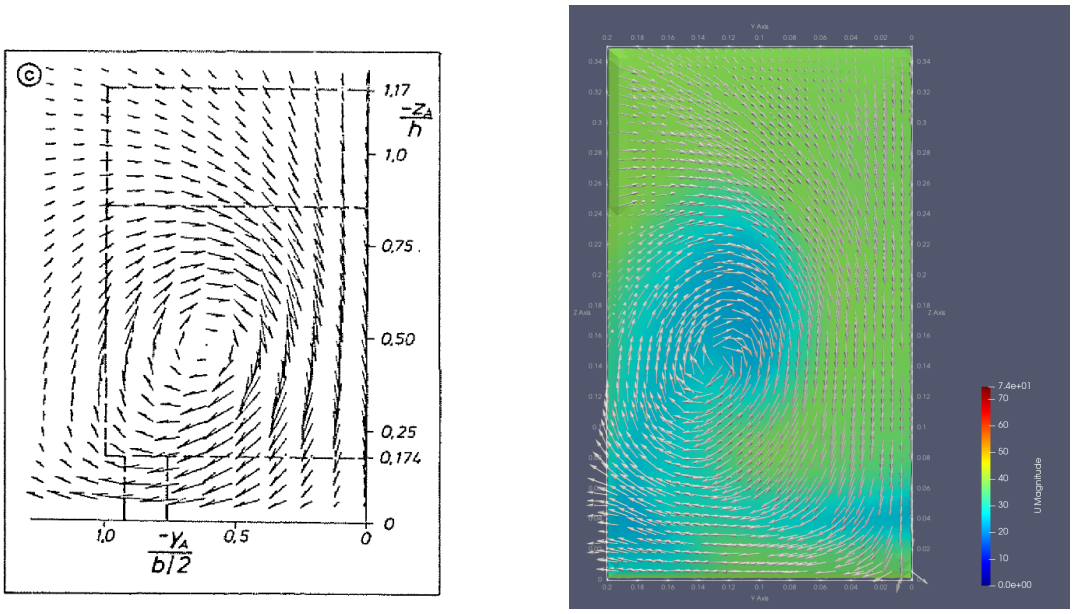

Figure 3.11: Mean flow velocity vector field and U velocity component magnitude at $x_a/l = -0.479$ (mesh 3).

Regarding Figure 3.9 the mean flow velocity vector field and U velocity component magnitude at $x_a/l = -0.077$ in either the Ahmed study and the present work can be seen, on the left and right side respectively. The Ahmed diagram shows the formation of a vortex around $-z_a/h = 0.8$ as well as a recirculating zone between $-z_a/h = 0.174$ and $-z_a/h = 0.75$. Both of these areas can be seen in the present work diagram; the vortice can be seen faintly in colour but the vectors clearly mark its presence.. As for the recirculating zone, there are a number of vectors that converge towards a specific line that

delimits the area of the said zone.

Similarly, Figure 3.10 presents the mean flow velocity vector field and U velocity component magnitude at $x_a/l = -0.190$ of both works, on the left and right side respectively. Here, in the Ahmed diagram, the vortice has developed further increasing its size and moving downward on the body and the recirculating zone is beginning to disappear although it still exists. In the present work, the vortice has followed the same behaviour as in Ahmed's increasing its size and moving downward. The recirculating zone, can still be seen although it does not have the presence it had at $x_a/l = -0.077$.

Finally, Figure 3.11 presents the mean flow velocity vector field and U velocity component magnitude at $x_a/l = -0.479$. Once again, the Ahmed diagram shows a vortice free of any flow structure (like the previous recirculating zone) and with a bigger size and moving downwards on the body. In the present work, the same behaviour is observed in the results, bigger size and a motion towards a lower part of the body.

With these three pictures one can conclude that the results are similar within margin of error to the experimental study of Ahmed. The results include, not only, the flow structures represented as well as their evolution along the wake of the body validating thus, the the present work CFD solution for a road vehicle, in this case, the Ahmed body.

3.5.3.2 Drag Coefficient

In this topic, Meile et al[25], propose a curve fit based on three sets of empirical data and plot a curve of the drag coefficient versus the Reynolds Number at 25°slant angle with a $R^2 = 0.9997$ which takes the following form,

$$C_D = 0.2788 + 0.0915 \cdot e^{-Re \cdot 10^{-6}/1.7971} \quad (3.6)$$

Table 3.5 contains the relevant parameters to calculate the theoretical drag coefficient such as the velocity magnitude, the kinematic viscosity of the air and the body length.

Table 3.5: Theoretical Scalar Quantities.

U	40 m/s
ν	1.48E-05 m²/s
Length	1.044 m
Reynolds Number	2.8E+06
Drag Coefficient (Theoretical)[25]	0.298

The present CFD results are shown in Table 3.5 and were obtained by averaging the last

200 iterations after a stable convergence as been reached. In Table 3.6 the drag coefficient converges towards the theoretical value as the mesh gets finer. On meshes 3 and 4, the result is mostly within the same margin of error and therefore one can assume to have hit mesh convergence.

Table 3.6: Drag Coefficient of the meshes.

Mesh	C_D	Error
1	0,35802	20.13%
2	0,32684	9.67%
3	0,30554	2.52%
4	0,30566	2.56%

3.5.3.3 Mesh y^+ evaluation

Using the post-process utility *yPlus* the minimum, maximum and average y^+ of each mesh could be otained.

As stated before, a $y^+ > 40$ was targeted to make use of wall functions implemented in *OpenFOAM*. This required the layers within the mesh to be crafted with care since most of times the y^+ values floated between 20 and 30 which requires trial and error.

Table 3.7: Y^+ of each mesh.

Mesh	Mininum	Maximum	Average
1	4,48564	1403,5966	212,06617
2	4,63691	810,19335	85,0436
3	2,13454	390,9107	42,879
4	2,30255	391,4056	42,859

As seen in the Table 3.7, y^+ kept getting lower with the refinement of the mesh until mesh 3 where it stayed mostly the same. Although the mesh kept getting finer, some cells presented a unnatural behaviour that could not be avoided such as the ones shown in Figure 3.12. These cells were responsible for driving the maximum value of y^+ to the 300 mark. However, since they only represent a small percentage of the total cells of the body and the presented CFD validation data followed closely the Ahmed Body experimental data, it can be assumed that the error caused by them was negligible.

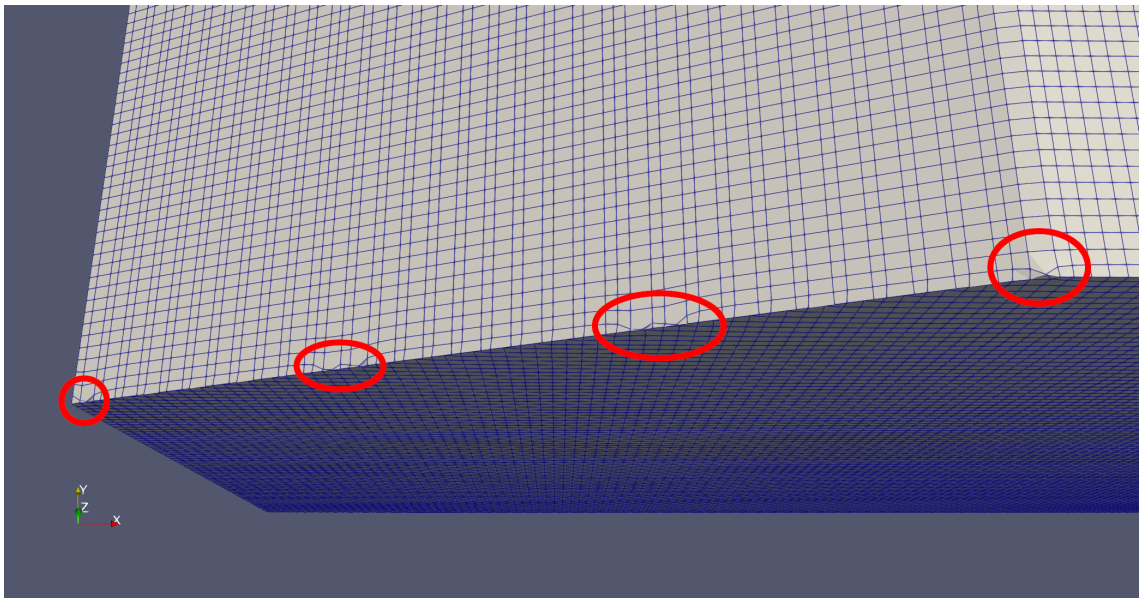

Figure 3.12: Cell distortions in the slant border (mesh 3).

3.5.3.4 Simulation Run Time

Simulation run times were compared between each mesh in order to assess which one had the best characteristics for vehicle simulation. In Table 3.8, a comparison between the different run times of each mesh is given. Let it be noted that although the comparison of the run time is made at 1500 iterations, most of the simulations took more time to converge. The 1500 mark is the minimum common iteration shared by all simulations.

Table 3.8: Run time of each mesh (1500 iterations).

Mesh	Run time [s]
1	381.57
2	2517.42
3	12855.94
4	27234.31

3.5.4 Mesh Choice

From the results obtained Figure 3.13 refers to the drag coefficient error versus the number of cells.

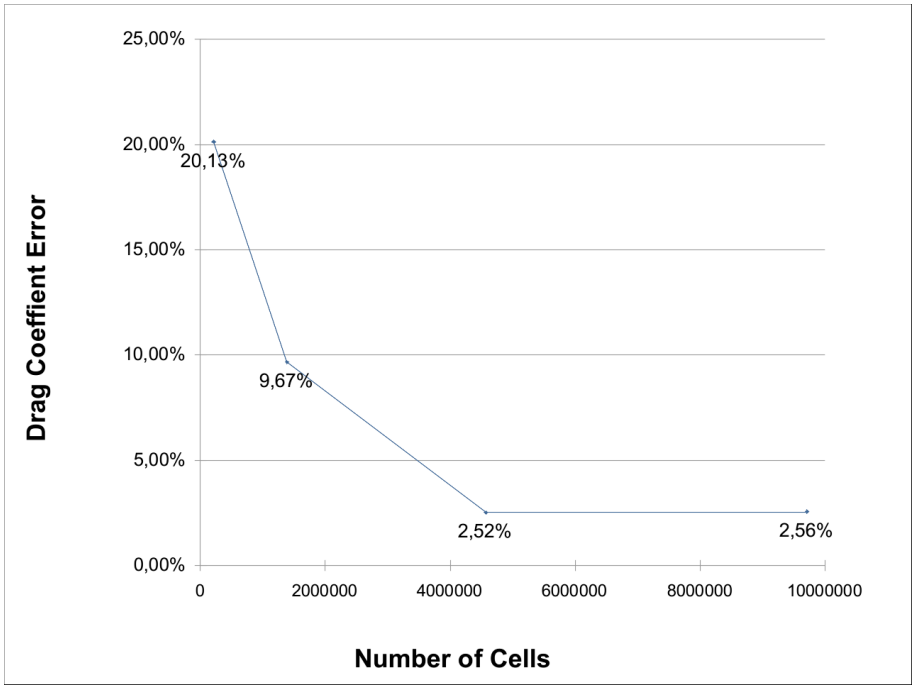

Figure 3.13: Drag Coefficient error versus Number of Cells.

By analysing Figure 3.13 one can derive that only mesh 3 and mesh 4 are suited for simulation since only those present a an error within an acceptable margin of 5%. With this conclusion, since both of them present almost the same error, mesh 3 was chosen as the best case because it provides a better compromise between simulation run time and error as it is the faster simulation between 3 and 4. Thus a target of approximately 5 million cells and a y^+ of 40 are the desired characteristics for the Shell Eco-Marathon 2019 car mesh.

3.6 Shell Eco-Marathon prototype

3.6.1 Case setup

3.6.1.1 Geometry

The Aero@UBI03 has a tadpole vehicle tricycle configuration, low frontal cross-section area monoseater with 2.7 meters in length by 0.68 meters wide and 0.55 meters tall. The competition vehicle is designed and built according to the 2019 Shell Eco-Marathon Rules and having competed in the 2019 Marathon edition it satisfies all requirements present in the rulebook. Figure 3.14 shows the vehicle virtual model in an isometric perspective.

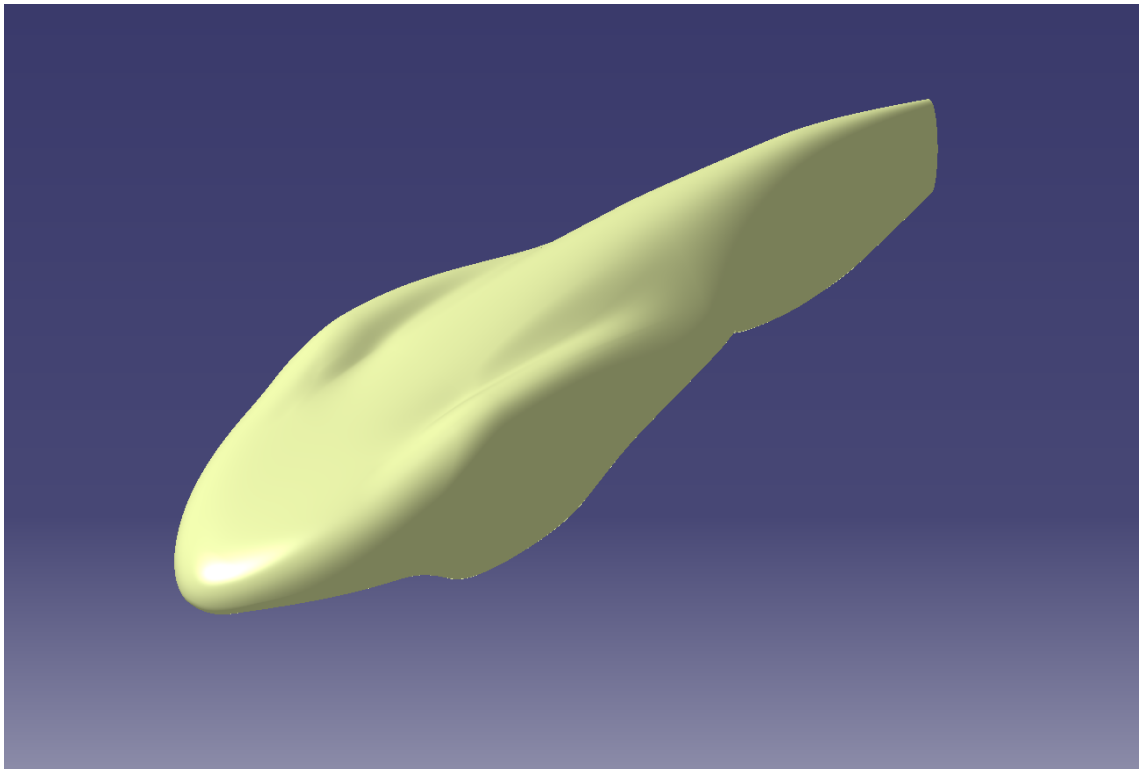

Figure 3.14: Isometric view of the prototype.

Before setting up the case in *OpenFOAM*, a geometry check up had to be done. The vehicle's STL, provided by the Aero@UBI Shell Eco Marathon team required a few modifications before it was ready for simulation. This involved the closure of all open faces such as, for example, the back side of the vehicle, as well as the addition of three, five millimeter pads below the wheels as seen in Figure 3.15. These pads prevent cell skewness during meshing because, at the moment of mesh creation, *SnappyHexMesh* has a simple square shape to mesh around instead of a complex convex shape.

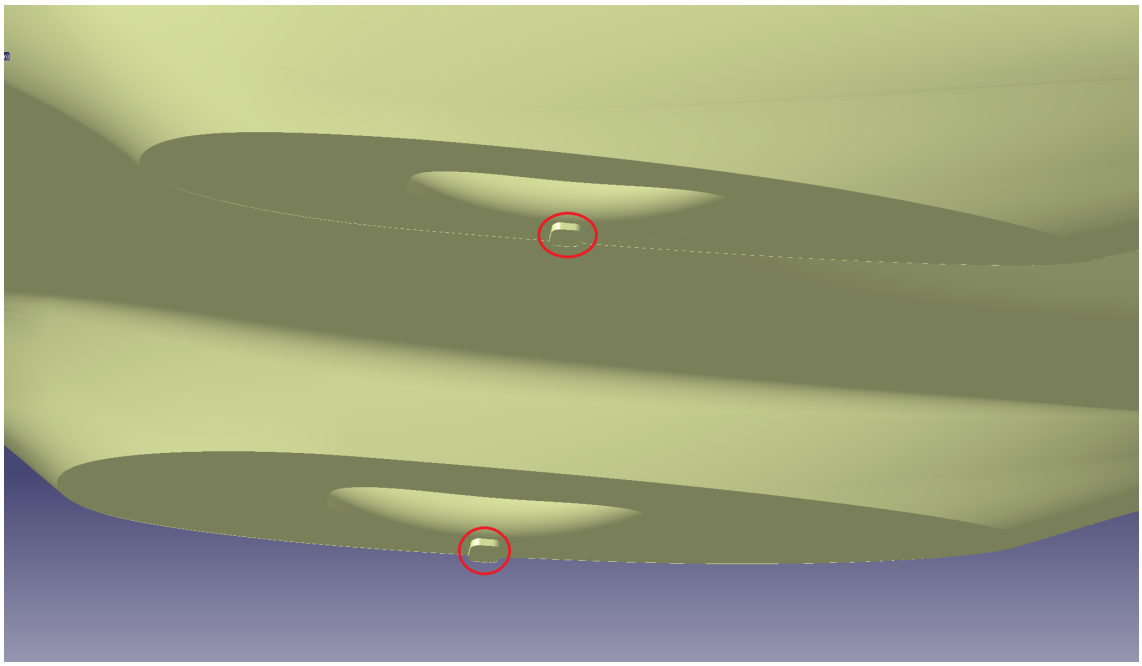

Figure 3.15: 5 millimeter pads below the wheels.

With the geometry processed, the case was setup according to the procedure described in Chapter 3.5.2.

3.6.1.2 Boundary Conditions

Similarly to chapter 3.5, the set boundary conditions are:

- Inlet velocity 7 m/s
- Pressure outlet set to 0 Pa
- Ground velocity set to 7 m/s
- Symmetry conditions on the side and top boundaries

For the turbulent boundary conditions, using the Equations 3.1 and 3.2 the values in Table 3.9 were set,

Table 3.9: Turbulent boundary conditions.

Freestream Velocity (u_{ref})	7 m/s
Turbulent Intensity (I)	1%
Turbulent kinetic Energy (k)	0.00735
Turbulent Length scale (l)	1.30 m
C_{μ}	0.09
Specific rate of dissipation (ω)	0.1204

3.6.1.3 Meshing

With the mesh parameters evaluated and validated, the mesh for the SEM prototype could be constructed. Thus, using the methodology described in Chapter 3.4, the resulting mesh has the characteristics shown in Table 3.10. A close up of this mesh can also be seen in Figure 3.4.

Table 3.10: Aero@UBI03 Shell Eco-Marathon 2019 Prototype mesh characteristics

Cell Size			Body Refinement		Layers		Mesh Statistics		
X	Y	Z	Vehicle	6 6 + line 6	N Layers	1	Points	Cells	Faces
0.3	0.302	0.302	Box	5	Expansion Ratio	1.05	5927643	5532017	16971644
			Box 2	4	Final Layer Thickness	2			

The number of layers stated in Table 3.10 is referring to the initial parameters set in *SnappyHexMesh*, four more layers were added using *refineWallLayer*.
Lastly, for the present work, the following simulations were ran:

- Normal, unchanged vehicle simulation
- Three cases where the angle of attack is incremented by 1°every iteration
- A case where the vehicle angle of attack was changed to 3°and was cut horizontally at the fairing section in order to make it touch the ground
- A case where the vehicle is lifted off the ground to access the ground effect influence

3.6.1.4 Convergence

As can be seen in Figure 3.16, the solution failed to converge at the 10^{-5} mark. However, the residuals stabilized after the 1400 iteration and created a periodic behaviour. Similarly, the forces plot in Figure 3.17 fully stabilized around the 800 iteration mark and entered a periodic behaviour. Even though, convergence through residuals was not achieved, these results are valid due to their periodic nature meaning the solution converged as much as it could.

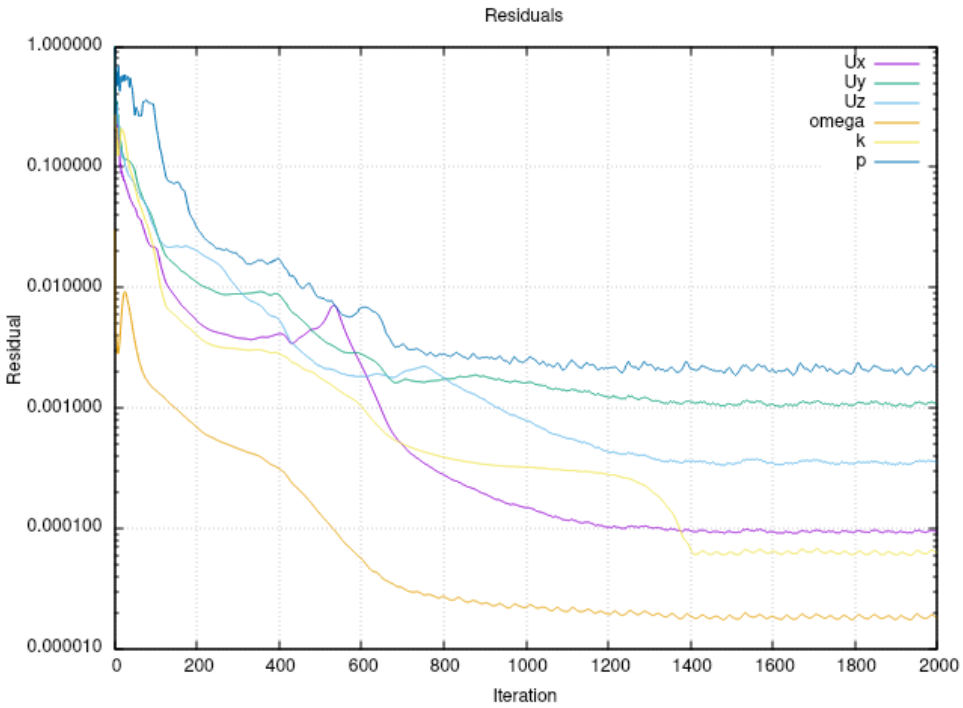

Figure 3.16: Residuals plot.

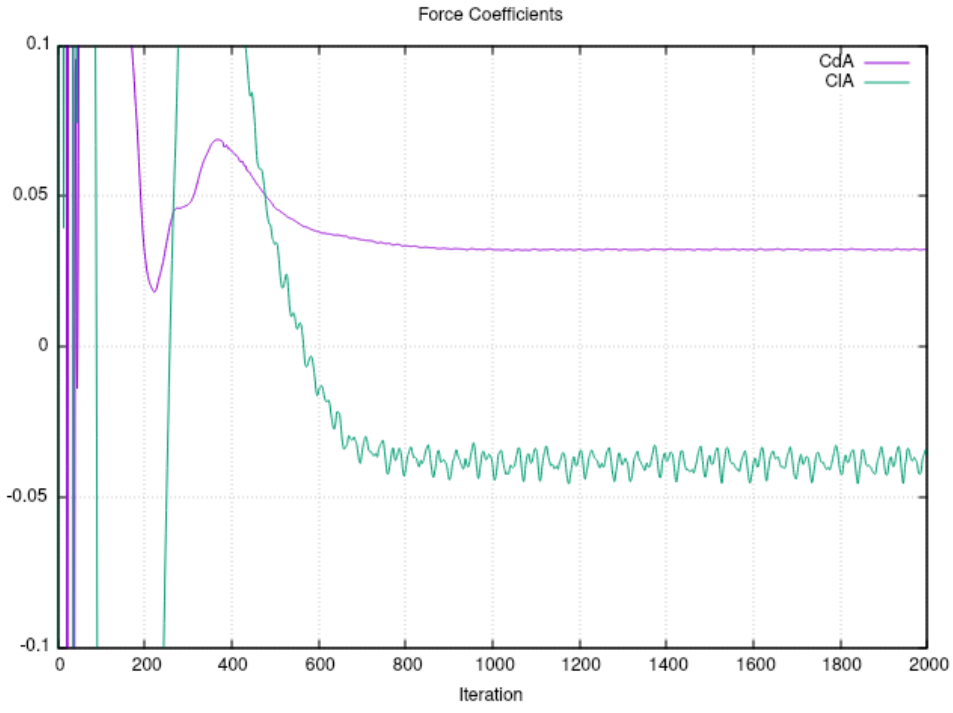

Figure 3.17: Forces values plot as Drag area, SC_D and Lift area SC_L values in m^2 .

Chapter 4

Results and Discussion

Although the present vehicle flow results presented have an entire CFD validation process behind them, these numerical results are not to be taken as granted. The main reason for this claim is the fact that there are no empirical wind tunnel data of the Aero@UBI03 vehicle to compare to and the process does not take into account all real life variables such as the actual vehicle construction process, all the cavities and irregularities in the real vehicle's surfaces. As such all the values shown here are an optimistic guess based on ideal conditions.

4.1 Aerodynamic Forces

In this section drag and lift results are presented. Figure 3.17 shows both SC_D and SC_L plotted versus the number of iterations. During the early stages of the simulation, the values float wildly as *OpenFOAM* is still converging to the solution. Shortly after, both coefficients drop and rise followed by their rapid convergence at the 800 iteration where it fluctuates around a certain result. The mean value over the last 500 iterations was taken for both coefficients. Table 4.1 presents these results.

Table 4.1: Comparison table found in [1] with the present AERO@UBI03 vehicle added.

	AERO@UBI01	**AERO@UBI03**	Pac Car II	IDRApegasus	ARTEMIDe	Microjoule	Fancy Carol
S $[m^2]$	0.35220	**0.30683**	0.25400	0.25800	0.28400	0.31000	0.21000
C_D	0.08833	**0.10517**	0.07500	0.09300	0.10000	0.10000	0.12000
SC_D $[m^2]$	0.03110	**0.03227**	0.01905	0.02399	0.02840	0.03100	0.02520

Regarding the comparison between all these vehicles it must be noted that some of the prototypes are vehicles with more than ten years of age, this means that the rule book at the time had a lot differences compared to today's, e.g, the turning radius went from 25 meters to 8 meters which in turn led to a bigger steering angle of the wheels and bigger fairings to accommodate this larger angle.

4.2 Aero@UBI03 Flow Results

This section shows the flow results for the Aero@UBI03 Shell Eco Marathon vehicle prototype. Firstly, a cut at the symmetry plane ($y = 0$) is presented to show the velocity magnitude, as seen in Figure 4.1. Only the vehicle contour remains visible in order to have a better look at the results. The wake momentum deficit immediately calls our attention due to its shape. It is compromised of three areas, firstly, a possible recirculation region right after the vehicle cut off represented by the darker colour, secondly, an intermediate colour that suggests a separation region starting at the vehicle's rear-end and lastly, the brighter colour shows the fading wake. Also, its shape can be described almost as a rearward bident suggesting that two different phenomena are occurring, at the top and bottom of the vehicle.

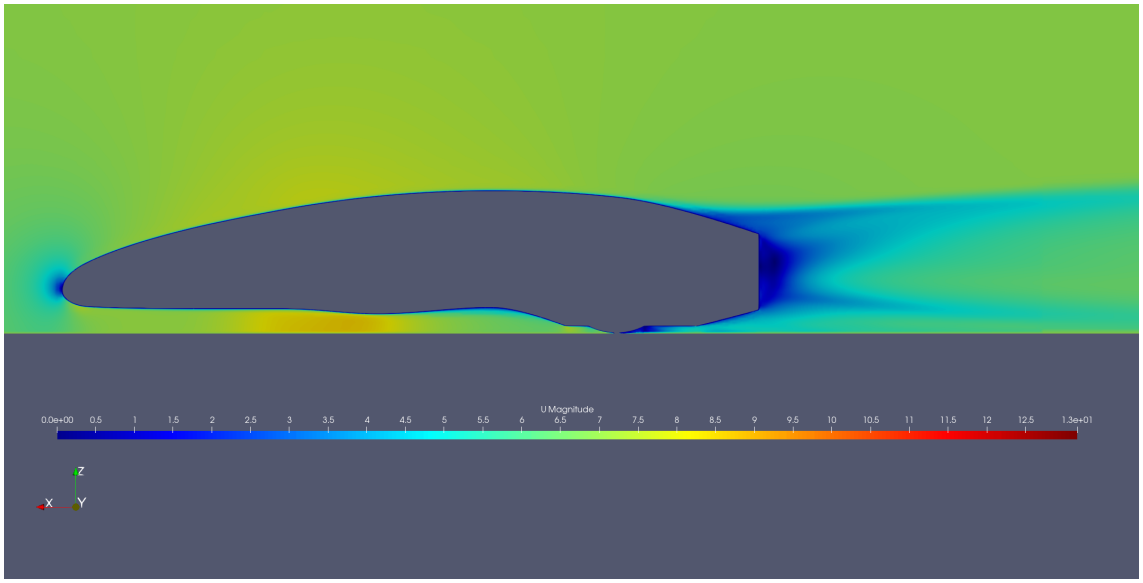

Figure 4.1: Velocity magnitude contour at symmetry plane.

First, lets analyse the flow at the bottom of vehicle. As seen in Figure 4.2, three distinct wakes can be seen coming from the wheels' fairings. The rear fairing, combined with the diffusive geometry at the vehicle bottom (behind the fairing) creates one of the bident spikes of the wake seen in Figure 4.1. Another possibility derived from Figure 4.2 is that the two fairings at the front each create a vortice, while the back fairing does not due to the simple shape of the wake. Alas, a closer inspection at the vehicle's wake through the velocity vector field located at $x/L = -0.27$ (see Figure 4.3) confirms the existence of said vortices at the bottom of the vehicle.

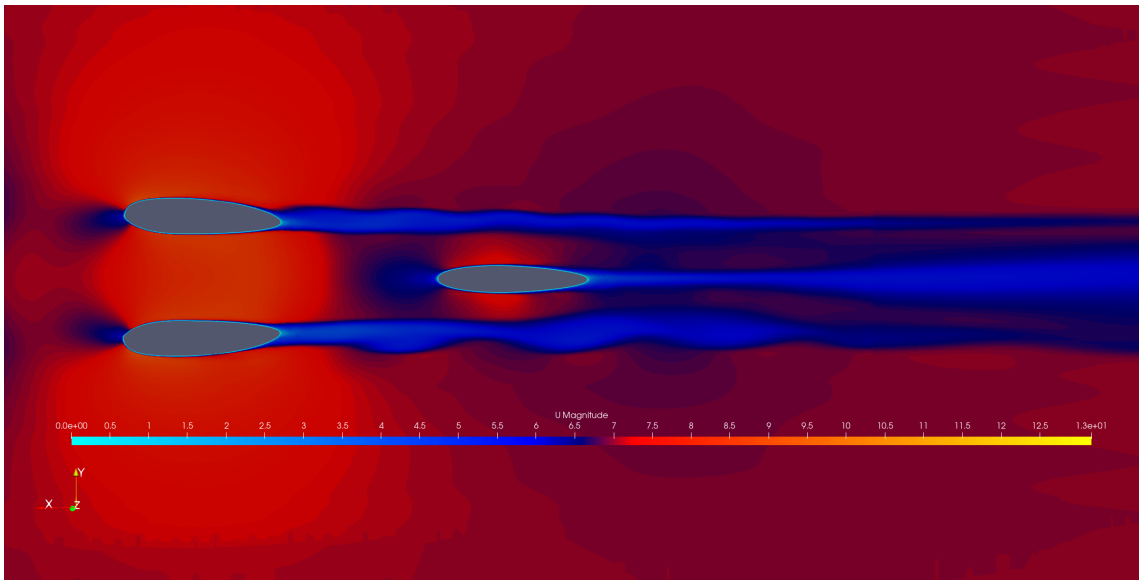

Figure 4.2: Velocity magnitude mean flow contour at $z = 0.0025$ m.

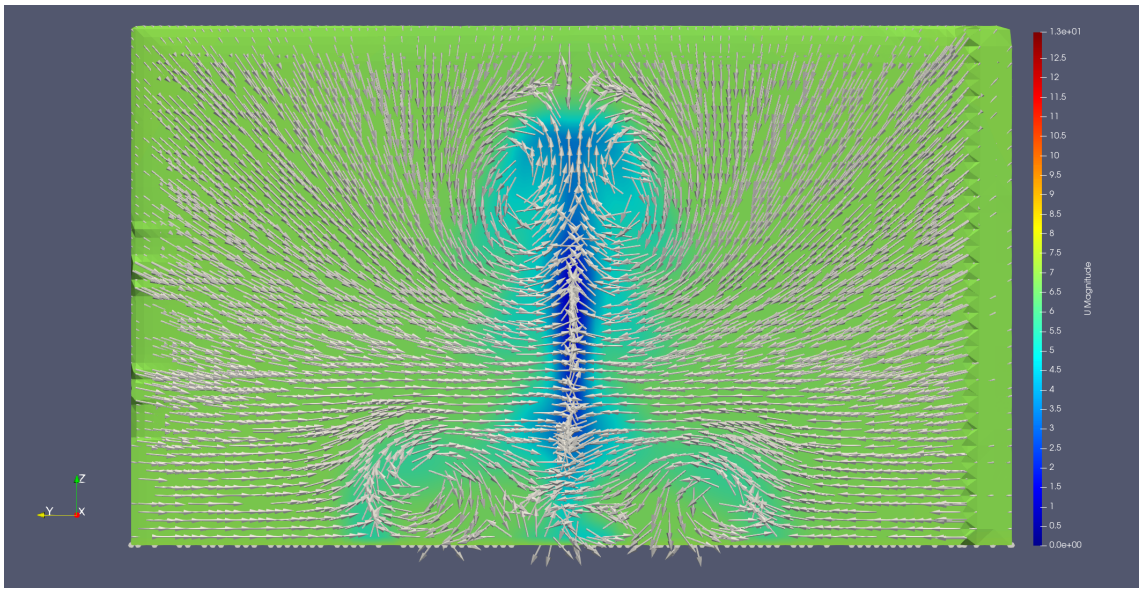

Figure 4.3: Velocity vector and velocity magnitude field at $x/L = -0.27$.

Secondly, Figure 4.3 also shows the existence of two other vortices located at the top of the vehicle. This is confirmed when looking at the Q-criterion isosurfaces shown in Figure 4.4. As such, four vortices can be seen, two, in a lower position generated by the front wheels fairings and the other two at the top of the vehicle. This is an important result as vortices are unwanted since they retain kinetic energy in the wake causing additional drag to the vehicle.

Thirdly, the cause of the top vortices needs to be investigated. By plotting the streamlines (see Figure 4.5 and 4.6), it can be seen that when the flow goes past the fairings, the flow closer to the vehicle curls when traversing to the latter half of the vehicle creating the

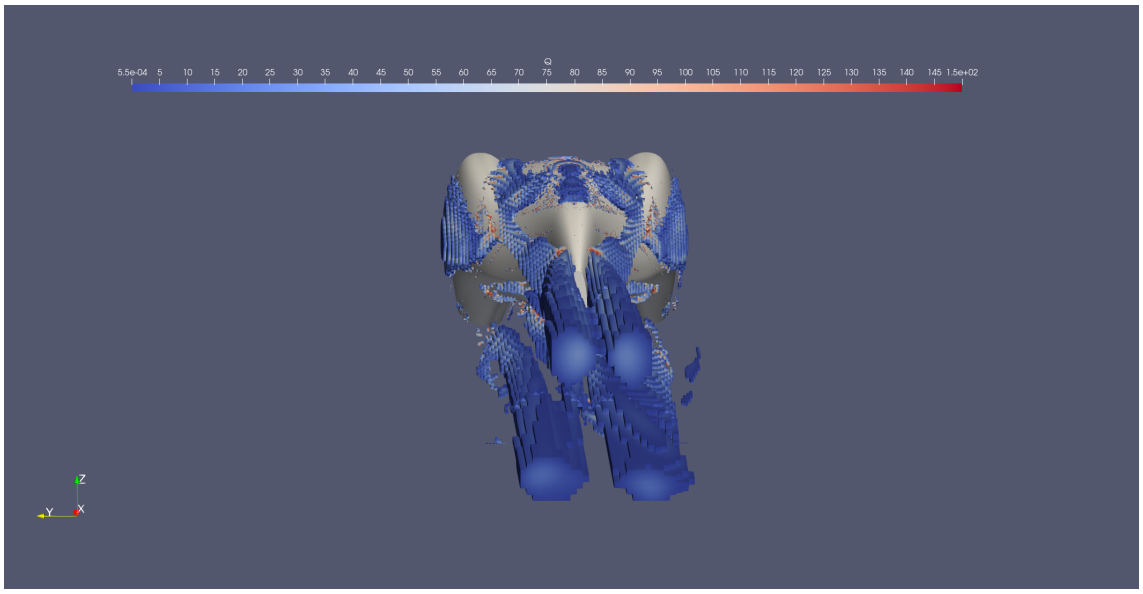

Figure 4.4: Iso-Countour of Q = 150 $1/s^2$

vortice. This is due to the geometry of the vehicle at the front wheels fairings. Since the philosophy design of the vehicle was to reduce the area of each section as much as possible, the fairings (since they could not be reduced) stand out like ”shoulders” of the vehicle, creating a small depression between the front wheel fairings and the middle section at the top of the vehicle. In conclusion, the interference between the sections and areas leads to the formation of the vortices in question.

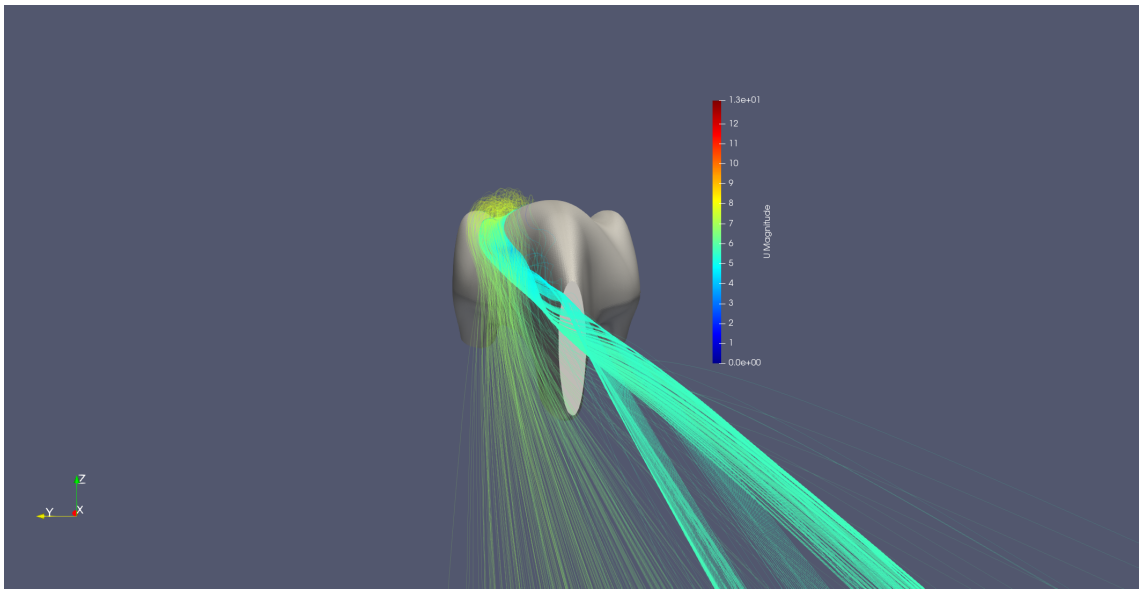

Figure 4.5: Rear-end view of the mean streamlines

Fourthly, in regards to separation, one can check it when the wall shear stress in the flow direction is negative. Hence, as seen in figures 4.7c ,4.7a and 4.7b, only behind the wheel exists separation.

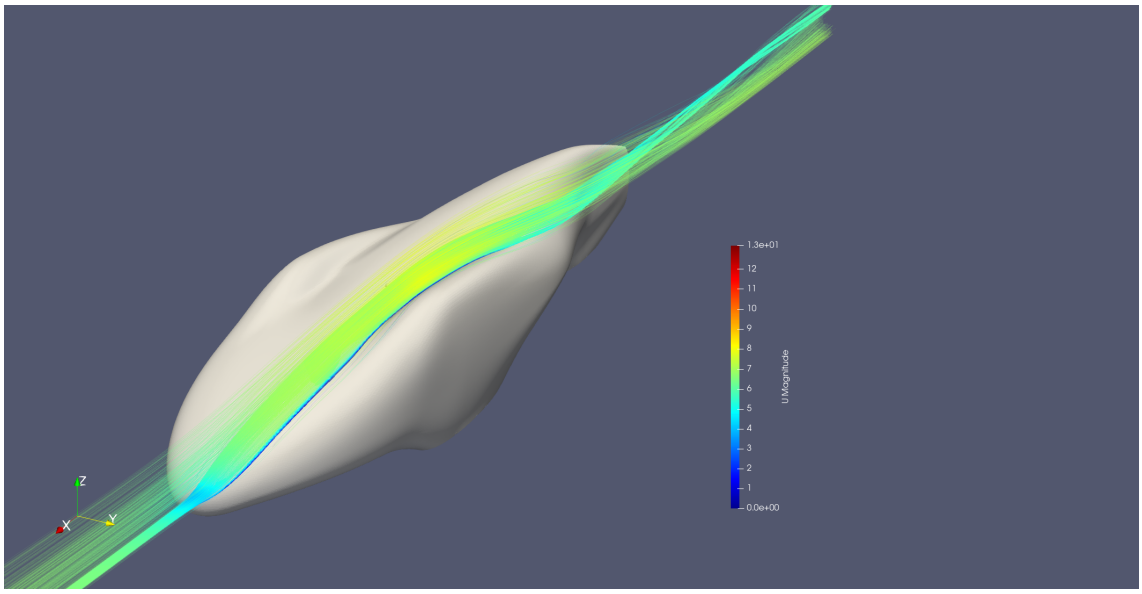

Figure 4.6: Isometric view of the mean streamlines

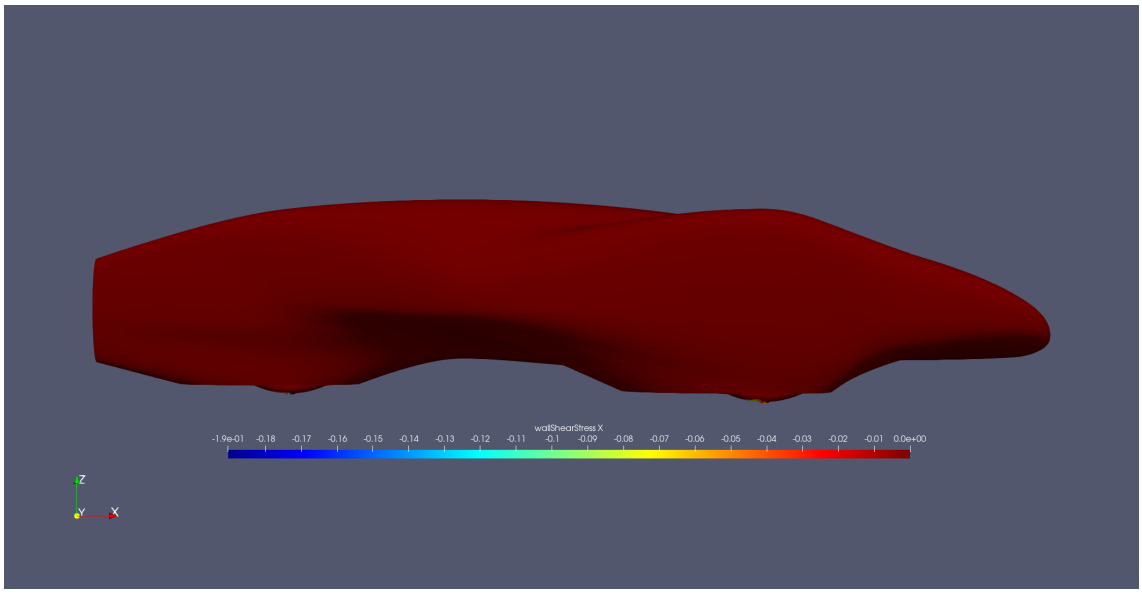

(a) Separation along the side.

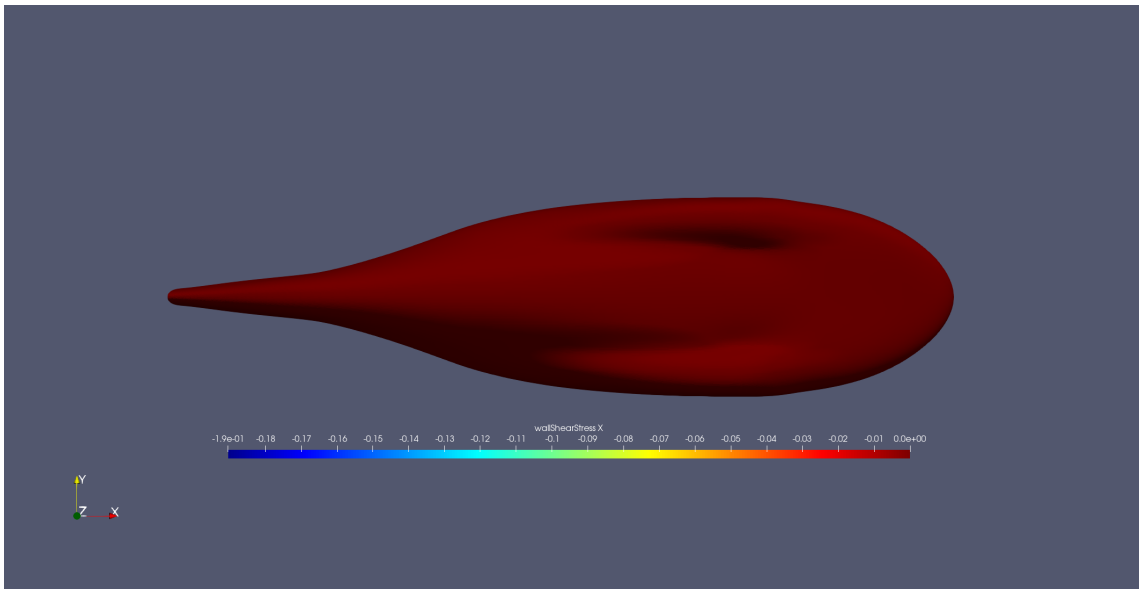

(b) Separation along the top side.

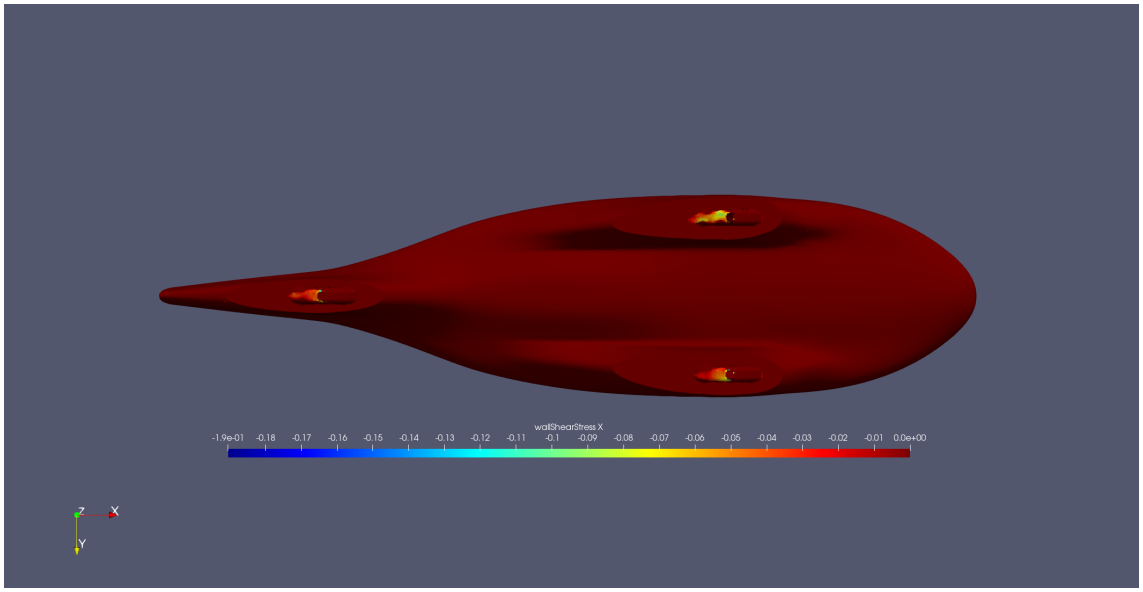

(c) Separation along the underside

Figure 4.7: Presence of negative wall shear stress on the vehicle indicative of flow separation.

Lastly, a small recirculation zone exists next to the rear-end cut of the vehicle as seen in Figure 4.8. Thus, we can conclude there is no separation in the vehicle's length at $7m/s$ and that the shape of the wake seen in Figure 4.1 is created by recirculation and the four vortices at the rear-end of the vehicle.

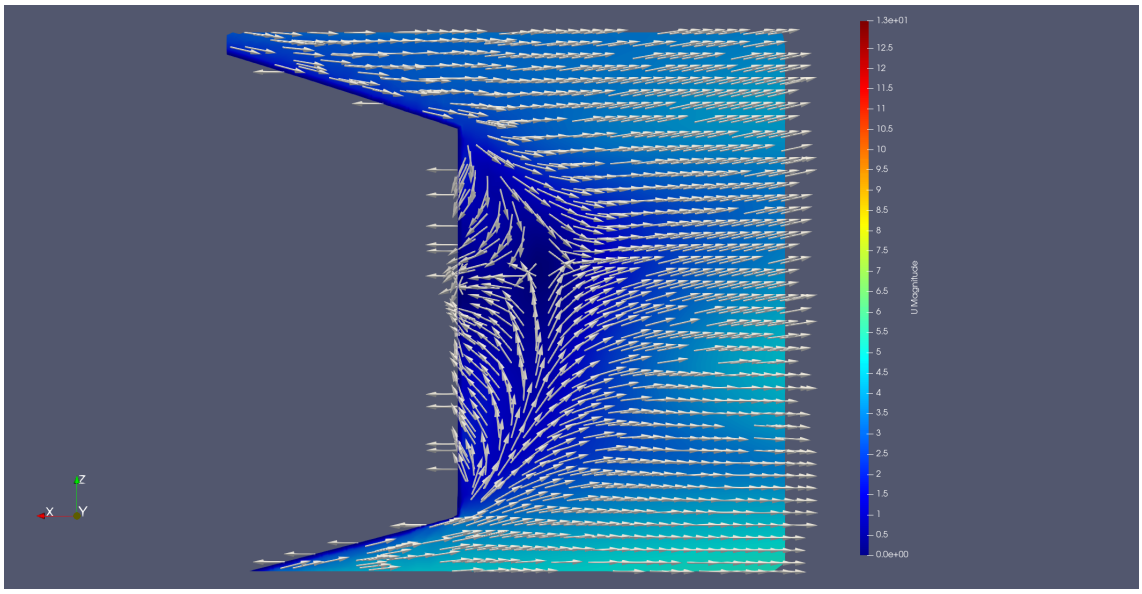

Figure 4.8: Velocity vector field and velocity magnitude detail located at the rear-end of the vehicle (symmetry plane)

4.3 Pressure Contour

The pressure distribution around the vehicle also provides key insight into its aerodynamics. Figure 4.9 shows the pressure contour. Here, three areas will be evaluated in further detail: the stagnation point located at the front of the vehicle, the low pressure zone in the middle of the car and finally the rear wheel fairing and rear-end of the vehicle. For the analysis, the pressure coefficient plot represented as Figure 4.10 will be used as a guide as it provides an important insight to how the pressure varies around the vehicle.

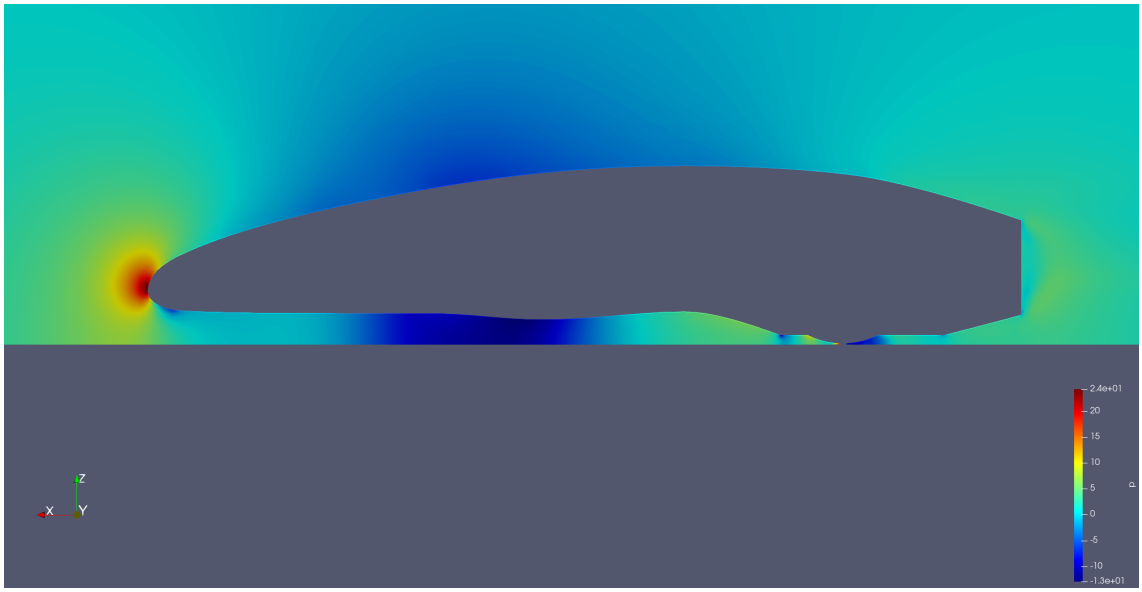

Figure 4.9: Pressure contour in the symmetry plane around the vehicle.

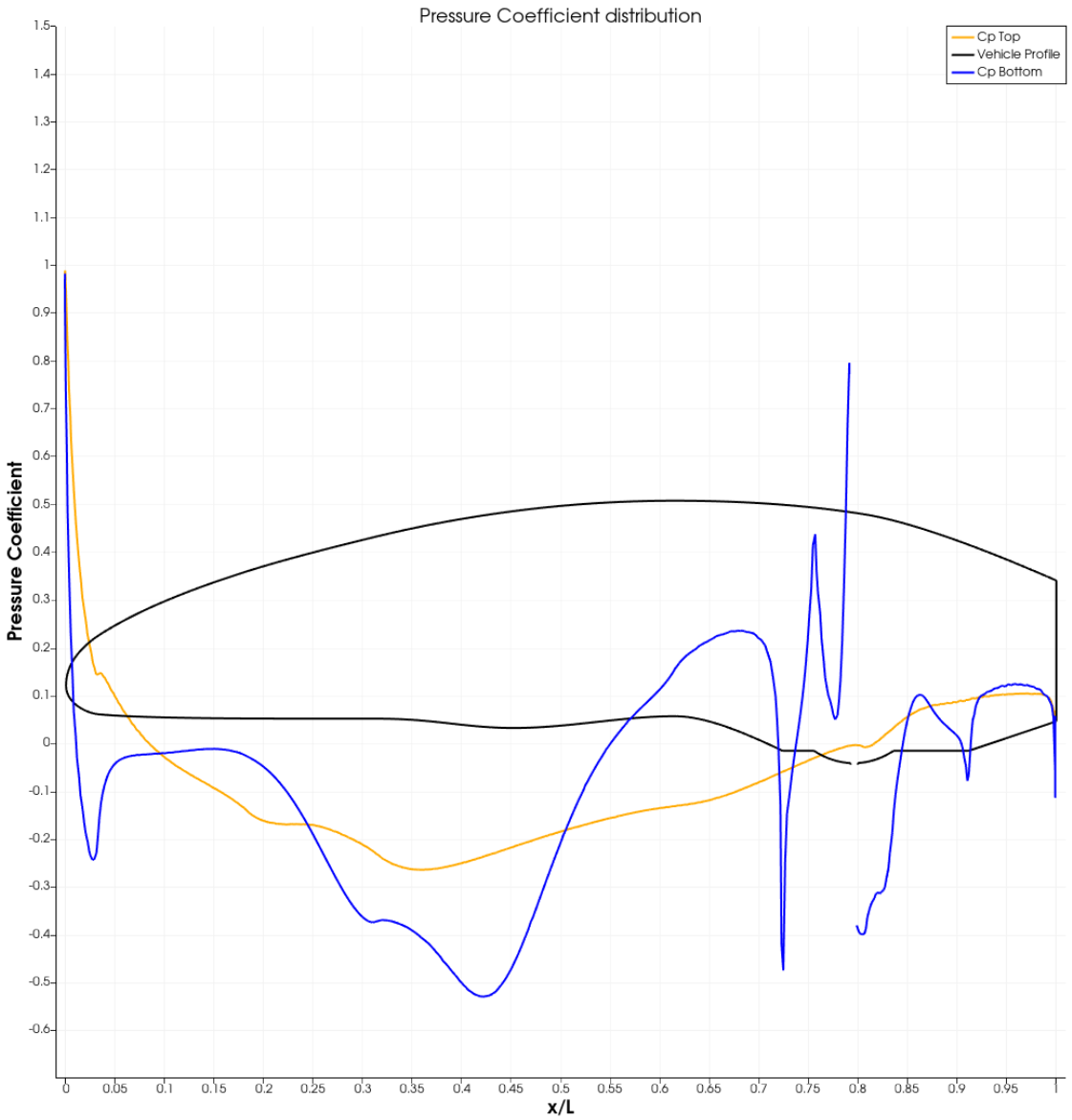

Figure 4.10: Pressure coefficient plot over the prototype.

The stagnation point as seen in Figure 4.11, is a point in a flow field were the pressure coefficient is one. Hence, in incompressible flows, the velocity at that point is null. Usually, one would not give much attention as it is a normal occurrence. However, on the lower side of the vehicle, between $x/L = 0$ and $x/L = 0.05$ as seen in Figure 4.10 we can see a sharp negative relative pressure. This suggests that the air accelerates generating extra unnecessary drag and negative lift, what may be indicative that the tip of the vehicle nose and the stagnation point are too high up in the body and might need to be lowered. Further analysis of this problem is done ahead in Subsection 4.4.

After the sharp pressure drop in the bottom of the vehicle, the relative pressure rises to less negative values and remains constant down to $x/L = 0.15$ before dropping to more negative values again. The pressure drop between $x/L = 0.2$ and $x/L = 0.55$ is the result

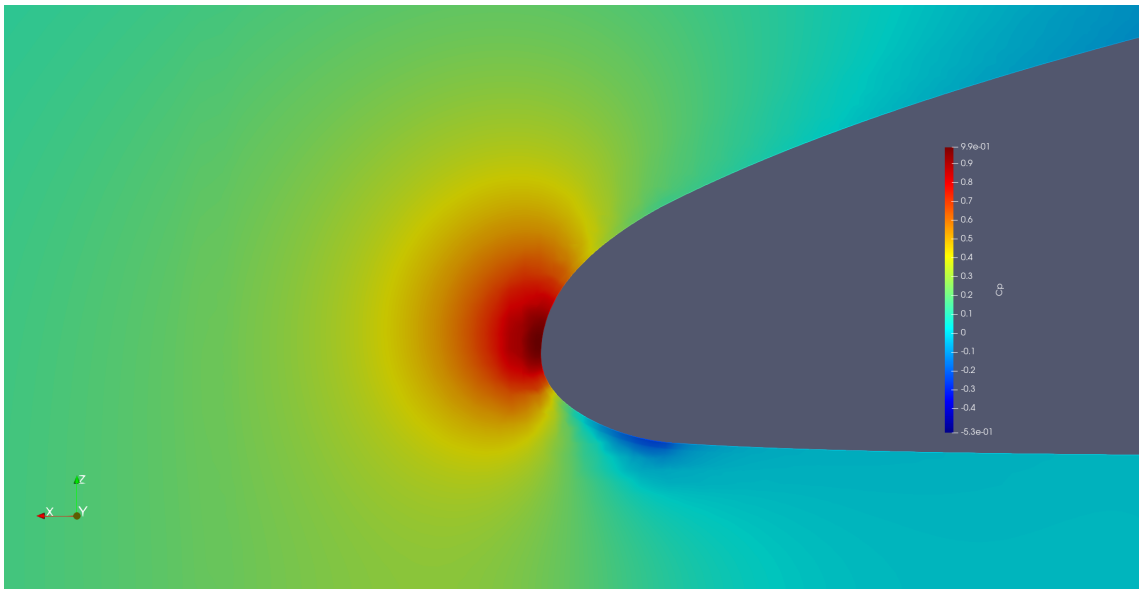

Figure 4.11: Stagnation point at the vehicles' front.

of a venturi effect between the two front wheel fairings generating, once again, additional downforce and drag. This is due to the front wheels fairings shape. Thus, one can conclude that improvements might be made by studying the effects of cambered front wheel fairings shapes to reduce this venturi effect in the bottom of the vehicle and possible downforce, thus reducing drag.

After the venturi effect, pressure recovers and goes as high as $Cp = 0.2$ before a sudden crash when transitioning into the rear fairing. Here pressure recovers again for a short length before stagnating completely due to the presence of the wheel. Finally, starting from $x/L = 0.8$, the pressure is low, again, behind the wheel. Here the pressure coefficient follows a diffusive behaviour due to geometry. As far as the upper body, pressure behaves as expected although a more smoother would be desirable.

4.4 Angle of Attack Influence on the aerodynamic forces

In this chapter, in an effort to eliminate the negative lift present in the original vehicle, the influence of the angle of attack will be studied as mentioned in Subsection 4.3. For this, three more test cases were run, each incrementing the angle of attack by 1°, three times from the starting vehicle position with the rear wheel always touching the ground.

Table 4.2 shows the lift and drag values for the study of the angle of attack influence. The lift area coefficients decreased as the angle of attack rose. The most significant change is the lift area coefficient that dropped by an order of magnitude at the 3°case. This is an expected behaviour since, as the angle of attack increases and, the pressure coefficient in

the underbody and in the upperbody increase (as seen in Figures A2, A3 e A4) thus, the lift area increases from negative values to almost zero, hence reducing the drag of the original vehicle as if the negative drag was causing some induced drag.

Table 4.2: Forces values results as Drag area, SC_D, and Lift area, SC_L, for each degree of angle of attack, values in m^2.

Angle	SC_D	SC_L
0°	0.03227	-0.03835
1°	0.03005	-0.02889
2°	0.02991	-0.01421
3°	0.03029	-0.00332

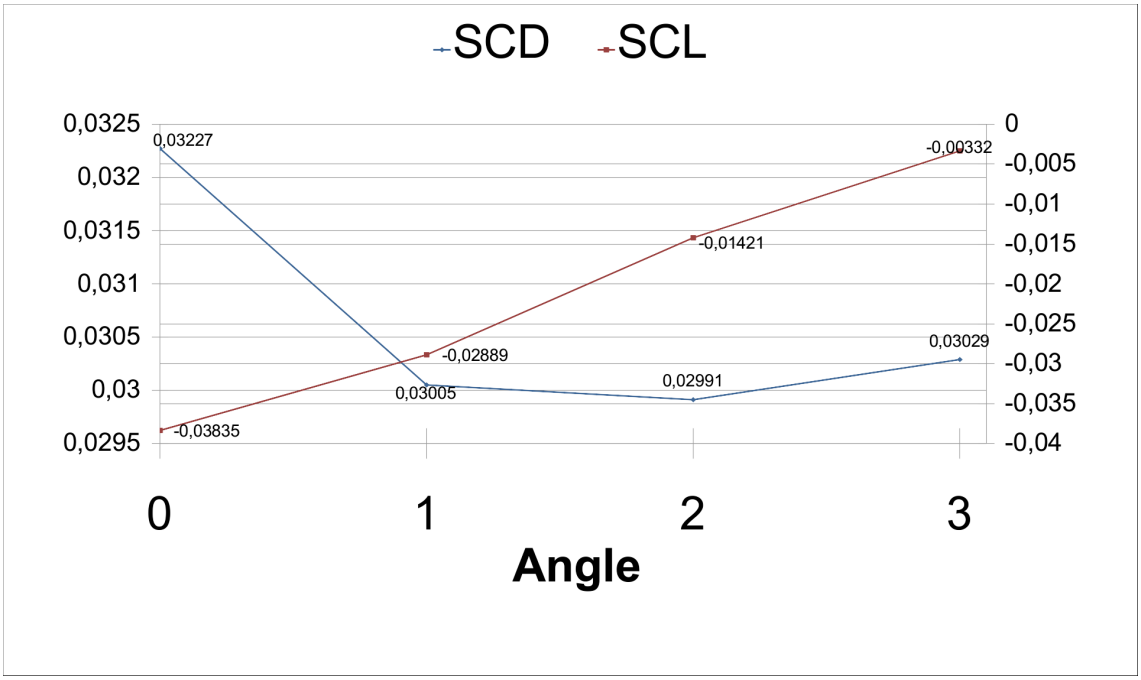

Figure 4.12: SC_D and SC_L plotted in function of the angle of attack.

A closer look at the stagnation point and each pressure coefficient plot (see Figure 4.13 and Figure 4.14, respectively) of each case shows that although the angle of attack was increased, it had almost no effect in the stagnation point location as it remains almost in the same position and that the subsequent sharp negative relative pressure at $x/L = 0.025$ did not see a large improvement. This leads us to believe that to change the stagnation point location one must either try and increase even higher the angle of attack or redesign the nose entirely.

Further analysis shows that the pressure at the front fairings decreases gradually, this is due to the attenuation of the ground effect because the vehicle is being lifted off the ground and the venturi effect created between the front wheel fairings diminishes.. In

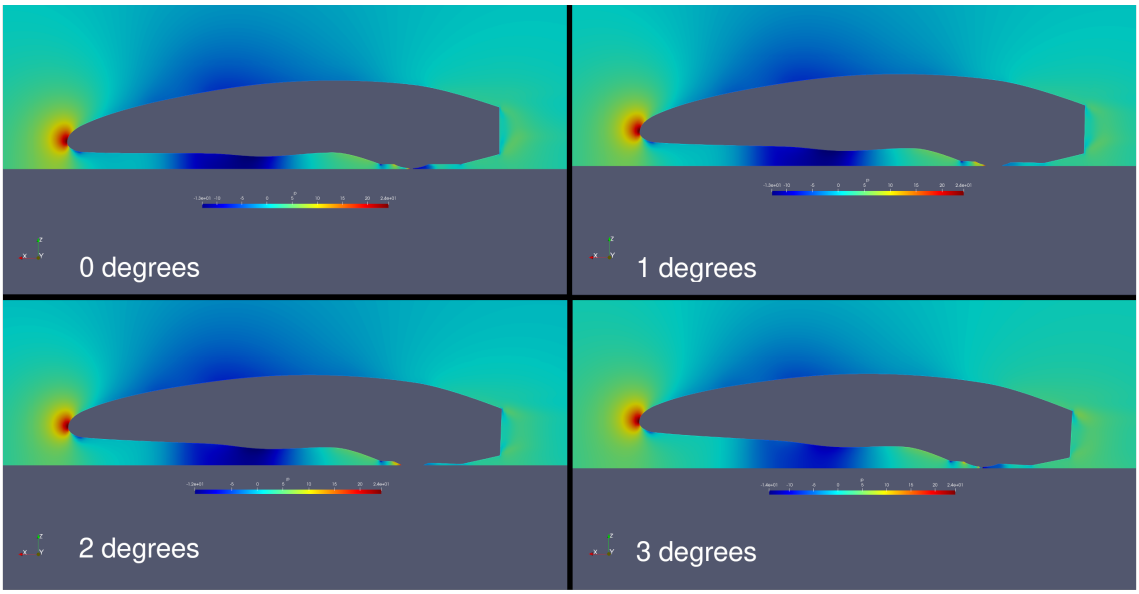

Figure 4.13: Pressure contour of all angles of attack.

conclusion, since the stagnation point had only a small effect on the pressure coefficient and thus the drag and lift area, the recorded changes regarding SC_D and SC_L come from the attenuation of both ground effect and the venturi effect.

4.5 Further Cases

Here the last two cases are discussed as they follow up the Subsection 4.4 analysis. The first case makes a horizontal cut at the fairings in the 3°angle of attack vehicle geometry in order to give the vehicle the desired incidence and to test it with all three wheels touching the ground as seen in Figure 4.15. Secondly, the original vehicle was raised with zero angle of attack the ground up to the height of the 3°angle off attack case. This is done to test if by raising the height of the vehicle a similar effect to the angle increase can be obtained in reducing the drag and negative lift of the vehicle. Like the other cases, the analysis is made based on the pressure coefficient plots (see Figure 4.16 and 4.17).

In the first case, as it can be seen in the pressure coefficient plot in Figure 4.16, the negative pressure coefficient magnitude right after the nose decreased by a great extent while the magnitude at the front wheel fairing region increased due to how close the vehicle is to the ground accentuating the venturi and ground effect . These results reflect themselves in Table 4.3 where the vehicle shows a substantial increase in SC_L and consequently in

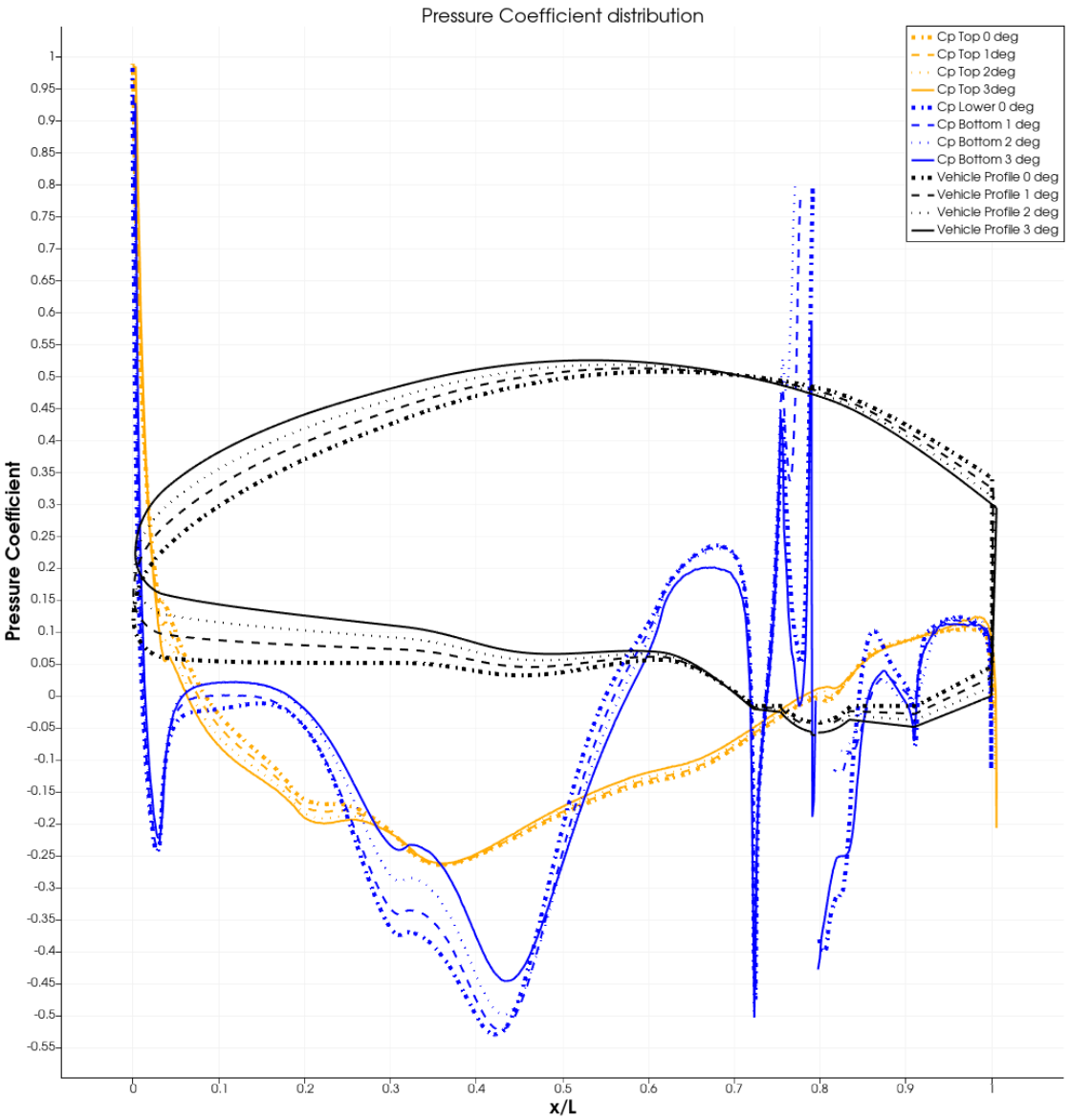

Figure 4.14: Pressure contour in the symmetry plane around the vehicle at different angles of attack.

SC_D. Although the result is not very relevant in dealing with the fairings problem, it sheds an important light in how to resolve the stagnation point showing that if given a couple more degrees of angle of attack are given, it can probably solve the pressure drop located at $x/L = 0.05$.

As far as the raising the original vehicle off the ground in a zero angle of attack attitude hypothesis goes, by analysing the pressure coefficient plot (see Figure 4.17) some conclusions can be drawn. Firstly, the stagnation point reverted to its initial behaviour but with a larger drop in pressure right below the nose and secondly, the venturi and ground effect at the wheel fairings decreased which lead to a decrease in the drag area coefficient as seen in Table 4.3. These two last cases helps us understand that most of optimization of this vehicle can be done by reducing the venturi effect at the front wheel fairings, by

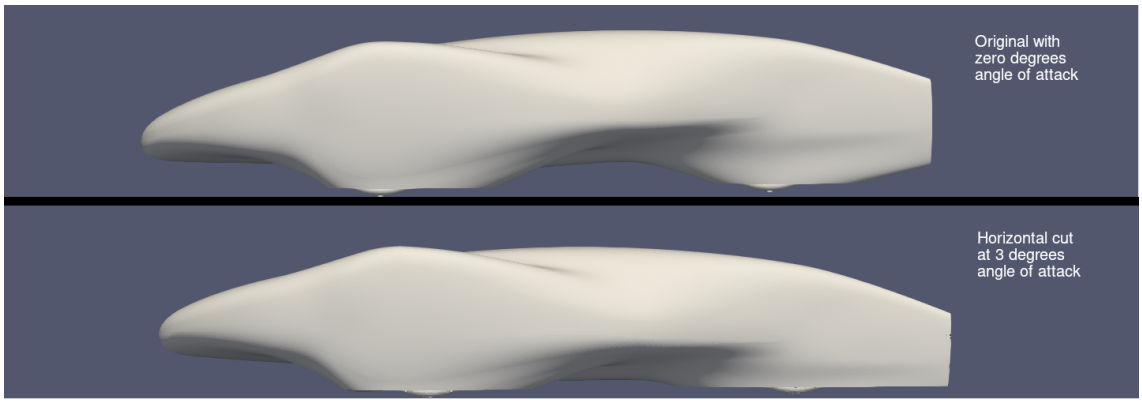

Figure 4.15: Comparison between the original vehicle and the new geometry after the horizontal cut in the 3°case.

cambering the fairings though a new full analysis would be needed.

Table 4.3: Drag and Lift area for each case.

Case	SC_D	SC_L
Original with 0°AoA	0.03227	-0.03835
Original with 3°AoA	0.03029	-0.00332
Horizontal cut at 3°	0.03237	0.03728
Raised from the ground	0.02888	-0.03117

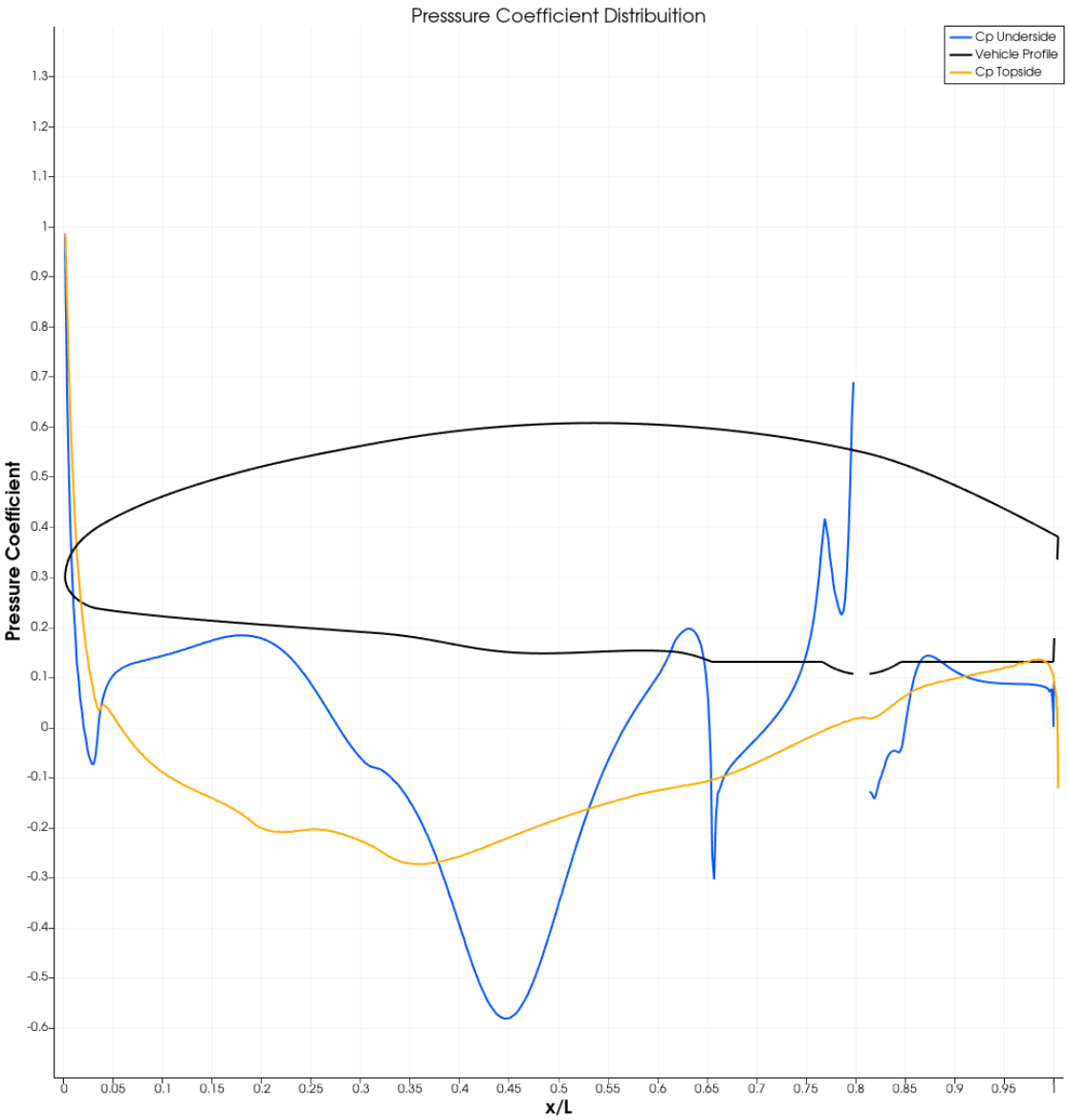

Figure 4.16: Pressure coefficient plot over the 3°cut vehicle.

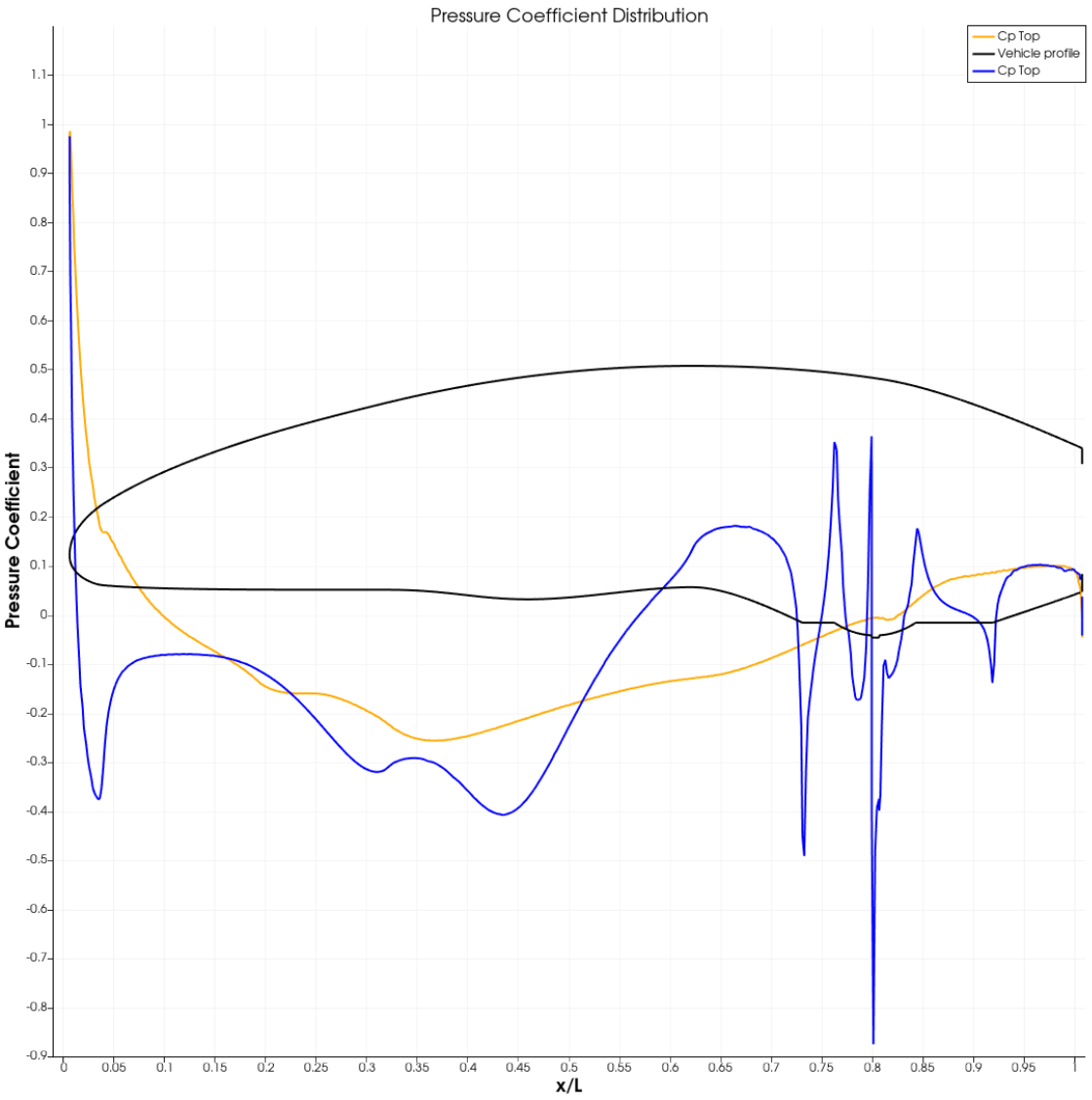

Figure 4.17: Pressure coefficient plot over the raised vehicle.

Chapter 5

Conclusion

In conclusion, a methodology to simulate the mean flow around the AERO@UBI03 vehicle with RANS CFD was successfully implemented and validated using the Ahmed Body present in the literature. The main contributions of the work are listed below:

- The creation of a OpenFOAM tools package workflow and methodology that suited the present and future works;
- The successful validation of the Ahmed Body using new parameters such as a moving floor, which helped the Aero@UBI03 simulation run accordingly the expected;

The main findings regarding the Aero@UBI03 prototype aerodynamics are:

- A total of four vortices generated by the vehicle. Two generated by the bottom front wheel fairings and the other two by the upper wheel fairings on the top of the vehicle;
- At the simulation parameters, no flow separation occurs;
- The frontal stagnation point seems to be located too high in the vehicle nose and a significant drop in pressure between the bottom front wheel fairings exists. These are responsible for a significant downforce in the vehicle;
- Analysis also showed that the geometry of vehicle in general should be simplified in areas such as the underside and top area between the front wheel fairings;
- SC_D analysis also suggests that a minimum exists, between 0 and 2 degrees of angle of attack, where the SC_D of the AERO@UBI03 would be lower than the AERO@UBI01 and Microjoule despite the more demanding turning radius of 8m of present day competition technical regulations that mandates wider front wheel turning angles;
- Further cases helped in the understanding of the influence of the front wheel and stagnation point effect on the drag and lift of the vehicle.

5.1 Future Work

Since the present work is done in an ideal environment with ideal parameters, it would be interesting to analyse the prototype in a full scale wind tunnel. This would allow the further validation of the methodology and provide an empirical comparison to the CFD case.

Further studies of the current vehicle can also be made by altering the geometry with the suggestions provided.

The next step of the project is to create a new CAD geometry based on the results found and evaluate its performance compared to the case in hand. If the suggestions are followed, a new vehicle geometry could be constructed with improved aerodynamic design.

Bibliography

[1] C. Magno dos Reis Fonte, "Design of a low consumption electric car prototype," Ph.D. dissertation, Universidade da Beira Interior, 2015. xiii, xv, 15, 41

[2] A. Cieslinski, W. Prym, M. Stajuda, and D. Witkowski, "Investigation on aerodynamics of super–effective car for drag reduction," *Mechanics and Mechanical Engineering*, vol. 20, no. 3, p. 295–308, 2016. xiii, 16

[3] Ahmed body. [Online]. Available: https://www.cfd-online.com/Wiki/Ahmed_body xiii, 26, 27

[4] S. Ahmed, G. Ramm, and G. Faltin, "Some salient features of the time-averaged ground vehicle wake," *SAE Technical Paper Series*, 1984. xiii, 26, 27, 30

[5] S. F. Hoerner, *Fluid-dynamics drag*. Pe Men Book Co., 1983. 5

[6] H. K. Versteeg and W. Malalasekera, *An introduction to computational fluid dynamics: the finite volume method*. Prentice Hall, 2011. 6, 13

[7] P. Spalart and S. Allmaras, "A one-equation turbulence model for aerodynamic flows," *30th Aerospace Sciences Meeting and Exhibit*, 1992. 8

[8] K. Hanjalić and B. E. Launder, "A reynolds stress model of turbulence and its application to thin shear flows," *Journal of Fluid Mechanics*, vol. 52, no. 4, p. 609–638, 1972. 8

[9] D. Wilcox, "Formulation of the k-omega turbulence model revisited," *45th AIAA Aerospace Sciences Meeting and Exhibit*, 2007. 8

[10] F. R. Menter, "Two-equation eddy-viscosity turbulence models for engineering applications," *AIAA Journal*, vol. 32, no. 8, pp. 201–213, 8 1994. 8, 17

[11] H. Kemal and B. E. Launder, *Modelling turbulence in engineering and the environment: second-moment routes to closure*. Cambridge University Press, 2011. 8

[12] F. Liu, "A thorough description of how wall functions are implemented in openfoam," 2016, edited by Nilsson. H. 13

[13] E. Abo-Serie, "Aerodynamics assessment using cfd for a low drag shell eco-marathon car," *Journal of Thermal Engineering*, vol. 3, no. 6, p. 1527–1536, 2017. 15

[14] Openfoam. [Online]. Available: http://www.openfoam.com/ 17

[15] Gui. [Online]. Available: https://openfoamwiki.net/index.php/GUI 17

[16] K-omega implementation. [Online]. Available: https://www.openfoam.com/documentation/guides/latest/doc/guide-turbulence-ras-k-omega-sst.html 18

[17] Paraview. [Online]. Available: https://www.paraview.org/ 20, 22

[18] B. Blocken, "Computational fluid dynamics for urban physics: Importance, scales, possibilities, limitations and ten tips and tricks towards accurate and reliable simulations," *Building and Environment*, vol. 91, p. 219–245, 2015. 22

[19] omegawallfunction. [Online]. Available: https://www.openfoam.com/documentation/guides/latest/doc/guide-bcs-wall-turbulence-omegaWallFunction.html 24

[20] nutuspaldingwallfunction. [Online]. Available: https://www.openfoam.com/documentation/guides/latest/doc/guide-bcs-wall-turbulence-nutUSpaldingWallFunction.html 24

[21] kqrwallfunction. [Online]. Available: https://www.openfoam.com/documentation/guides/latest/doc/guide-bcs-wall-turbulence-kqRWallFunction.html 24

[22] Openfoam v6 user guide: 4.4 numerical schemes. [Online]. Available: https://cfd.direct/openfoam/user-guide/v6-fvschemes/ 25

[23] Turbulence length scale. [Online]. Available: https://www.cfd-online.com/Wiki/Turbulence_length_scale 28

[24] Turbulence intensity. [Online]. Available: https://www.cfd-online.com/Wiki/Turbulence_intensity 28

[25] W. Meile, "Experiments and numerical simulations on the aerodynamics of the ahmed body," *CFD Letters*, vol. 3, no. 1, p. 32–39, Mar 2011. 32